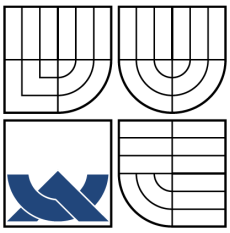

BRNO UNIVERSITY OF TECHNOLOGY
VYSOKÉ UČENÍ TECHNICKÉ V BRNĚ

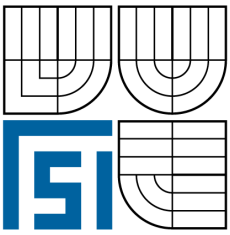

FACULTY OF MECHANICAL ENGINEERING
INSTITUTE OF PHYSICAL ENGINEERING

FAKULTA STROJNÍHO INŽENÝRSTVÍ
ÚSTAV FYZIKÁLNÍHO INŽENÝRSTVÍ

PLASMONIC ANTENNAS
PLAZMONICKÉ ANTÉNY

ABSTRACT OF DOCTORAL THESIS
TEZE DISERTAČNÍ PRÁCE

AUTHOR
AUTOR PRÁCE

Ing. MICHAL KVAPIL

SUPERVISOR
VEDOUCÍ PRÁCE

prof. RNDr. TOMÁŠ ŠIKOLA, CSc.

BRNO 2015

Summary
This doctoral thesis deals with plasmonic antennas. The resonant properties of plasmonic antennas are studied both theoretically and experimentally. Theoretical calculations are made using finite-difference time-domain numerical method in Lumerical FDTD Solutions software. For the experiments, antennas are fabricated by electron beam lithography. Resonant properties of the fabricated antennas are studied by Fourier transform infrared spectroscopy. The thesis is aimed at the investigation of the resonant properties of plasmonic antennas, when situated on a film of nanocrystalline diamond. Also, the application of antennas as a plasmon-based sensor functionalized to streptavidin sensing is investigated. Finally, an antenna with the shape of the letter V is introduced. Due to the reduced symmetry of the V-antenna, the incident light of wavelength close to antenna quadrupole mode is unidirectionally scattered.

Abstrakt
Tato disertační práce pojednává o plazmonických anténách. Rezonanční vlastnosti plazmonických antén jsou studovány teoreticky i experimentálně. Teoretické výpočty jsou prováděny v programu Lumerical FDTD Solutions užitím numerické metody konečných diferencí v časové oblasti. Pro experimentální studium byly antény vyrobeny pomocí elektronové litografie. Rezonanční vlastnosti vyrobených antén jsou studovány fourierovskou infračervenou spektroskopií. Práce se zaměřuje na studium rezonančních vlastností antén vyrobených na vrstvě nanokrystalického diamantu. Dále zkoumá možnost využití antén jako plazmonického senzoru funkcionalizovaného k detekci streptavidinu. Nakonec je představena anténa tvaru písmene V, u které dochází v důsledku porušení symetrie antény ke směrovému rozptylu dopadajícího světla. Tato směrovost se ovšem projevuje jen na vlnových délkách blízkých kvadrupólovému módu antény.

1 Introduction

Plasmonics is a major part of the field of nanophotonics. It deals with the interaction of electromagnetic radiation with conduction electrons at metal-dielectric interfaces including spatially limited (localized) interfaces of metallic micro and nanostructures. When proper conditions are met, conduction electrons of metals respond collectively to the incoming radiation, oscillate collectively and transform incident spatial electromagnetic waves into surface electromagnetic waves.

When the metal-dielectric interface is spatially limited to the dimensions below the wavelength of applied electromagnetic radiation, surface plasmons are confined to such limited interface; they are *localized*. The localized surface electromagnetic waves coupled to the conduction electrons oscillations are called localized surface plasmons (LSPs). Upon the illumination, standing electromagnetic waves arise in these subwavelength structures which leads to significant resonant effects at specific wavelengths – the enhancement of electric field in close vicinity of the structures and the enhancement of the light scattered by the structure. The latter has been widely utilized, albeit without any deep understanding of this effect, for staining glass since the times of ancient Roman Empire.

When structures exhibit the resonance of LSP due to external illumination, the incident electromagnetic field is concentrated by the structure to a small zone around the structure. This feature makes them very similar to classical macroscopic electromagnetic antennas which are designed to concentrate the propagating electromagnetic radiation into a small and well confined space, where the power of radiation is either received or released by the antenna [1]. That is the reason why these resonant plasmonic structures are usually called *plasmonic antennas*.

In 1908 Gustav Mie published his seminal paper on light scattering and absorption by spherical metallic particles [2]. In the paper, Mie developed complete analytical theory for the description of interaction of metallic sphere with incoming electromagnetic radiation and used this to solve one of the early 20^{th} century physical stumper – he managed to explain the colour of gold colloid particles. The size of gold nanoparticles exhibiting LSP resonance in the visible spectral region is between tens and approx. 180 nanometres (detached from substrate), so these dimensions were far below the resolution limit of the best available observation equipment of Mie's time – the bright field optical microscope (approx. 400 nm). So these particles remained hidden from direct observations. The only instrument which could make these particles visible was the *ultramicroscope*, the invention of Richard Zsigmondy, Henry Siedentopf and Zeiss Company [3].

The presented doctoral thesis deals with subwavelength plasmonic antennas. The work involves numerical computations and experimental studies of plasmonic antennas, their electromagnetic field in near- and far-field as well as the description of fabrication techniques and used materials. The thesis is aimed at the investigation of the resonant properties of plasmonic antennas, when situated on a film of nanocrystalline diamond. Also, the application of antennas as a plasmon-based sensor functionalized to streptavidin sensing is investigated. Finally, an antenna with the shape of the letter V is introduced. Due to the lower symmetry of the V-antenna, the incident light of wavelength close to antenna quadrupole mode is unidirectionally scattered.

2 Plasmonic antennas

As we have already mentioned in the introduction the structures which exhibit the resonance of localized surface plasmons due to the external illumination are often called plasmonic *antennas*, due to their similarity to macroscopic electromagnetic antennas.

An optical plasmonic antenna can effectively convert the energy of propagating radiation into the localized energy and vice versa. From microscopic point-of-view, the optical antenna effectively replaces a focusing lens (or an objective), as it concentrates the incident radiation to dimensions much smaller than diffraction limit. Unlike most of its radio- and microwave counterparts, the optical antenna can act both as a receiver for localizing of the incoming energy and as a transmitter for emitting of the optical response in the same time [1].

The main challenge of an efficient antenna design is the coupling of electromagnetic power flow between the near- and far-field of the source (or receiver). One of the most efficient antenna designs for optical frequencies are rod-like half-wave dipole antennas [4] and bow-tie antennas [5]. However, when one is interested in LSPR, then any metallic nanostructure can be viewed as an optical antenna [1]. For spectral regions, where metals act as a good conductor, the LSPR wavelength λ_r of half-wave dipole antennas can be estimated by modified formula for half-wave dipole

$$\lambda_{\mathrm{r},} \cong 2n_\mathrm{eff}L, \tag{2.1}$$

where λ_r is the resonant wavelength, n_eff is the effective refractive index (real part), L is length of the antenna.

2.1 Resonant properties of plasmonic antennas

Equation (2.1) represents a *geometrical* condition of existence of standing waves in the rod-like antenna. Another resonant condition, the *material* one, is represented by Fröhlich condition

$$\Re\{\varepsilon(\omega)\} = -2\varepsilon_\mathrm{m}. \tag{2.2}$$

When this condition is fulfilled, then the resonance effects are the biggest possible. The former condition (Eq. 2.1) means that for rod-like plasmonic antennas, there always exists the wavelength for which light scattering by the antenna as well as electric field in the antenna near zone is enhanced due to LSPR. Simultaneous fulfillment of Fröhlich condition (2.2) then increases the resonant effects, but it is not essential for the existence of LSPR in the antennas.

Therefore, by the term *resonant properties* of antenna we mean the wavelength of standing waves corresponding to dipolar polarization of antenna, i.e. the wavelength of LSPR, the value of antenna scattering cross section at LSPR and the value of enhancement of electric field in the close vicinity of the antenna at LSPR.

From the optical point-of-view, the consequence of LSPR, the enhancement of particle-light interaction is more interesting. The ability of particles to interact with electromagnetic radiation and thus to scatter or absorb the radiation is expressed by cross sections

for scattering C_{sca}, absorption C_{abs} or extinction C_{ext}. The cross sections are calculated from the density of power flux (expressed by Poynting vector $\vec{S} = \vec{E} \times \vec{H}$) in the vicinity of the particle. The scattering cross section has following form [6, p. 140], [7, p. 71]:

$$C_{\mathrm{sca}} = \frac{k^4}{6\pi}|\alpha|^2 = \frac{8\pi}{3}k^4 a^6 \left|\frac{\varepsilon - \varepsilon_{\mathrm{m}}}{\varepsilon + 2\varepsilon_{\mathrm{m}}}\right|^2 . \tag{2.3}$$

The Fröhlich condition can be seen again in the denominator of cross section, this implies that the cross sections have maximum values when the particle polarizability is at its maximum, i.e. at LSPR. The scattering efficiency scales with a^6 which makes it sometimes difficult to experimentally detect the scattering signal from very small particles.

2.2 Analytical models for resonance of rod-like plasmonic antennas

A classical antenna design assumes no time lag between the reactions of conductive electrons on incoming electromagnetic field. A consequence of this assumption is no penetration of electromagnetic field into the metal (no skin effect). However, at optical frequencies, the electromagnetic field penetrates into metals and skin effect cannot be neglected. The main result of this feature is that LSPR wavelength is no longer a simple function of the antenna geometry, like the one expressed by equation (2.1). Therefore, antenna dimensions cannot be directly scaled down from the radio- or microwave region to the optical one. The solution of this issue is possible by implementation of one of several analytical models like those in [8], [9].

Model of Kalousek [9] uses different approach to find the resonant wavelength λ_{r} of very thin antennas upon normal illumination. Using the quasi-static approximation (requesting $R \ll \lambda$) together with the assumption of uniform charge distribution over the transversal antenna cross section, the density of free-electron Lagrangian is calculated and then used in Euler-Lagrange equation, from which the wave equation is derived. From the wave equation, the phase velocity of longitudinal free-electron density waves (i.e. surface plasmons) is calculated and subsequently used for the determination of localized surface plasmon eigenfrequencies, i.e. frequencies of standing electromagnetic waves in the antenna. The final relation for resonant wavelength of a very thin antenna is then

$$\lambda_{\mathrm{r},j} = \frac{2\lambda_{\mathrm{p}}}{j\pi}\frac{L}{R}\left[\ln\left(\vartheta\frac{L}{R}\right)\right]^{-1/2} , \tag{2.4}$$

where $j = 1, 2, 3, \ldots$ is the mode of resonance and $\vartheta = 2\mathrm{e}^{-1/2}$. Moreover, model of Kalousek also deals with polarizability of thin antennas at resonance which is then used for the analytical expression of antenna near-field.

3 Used methods and techniques

3.1 Finite-difference time-domain numerical method

When resonance of plasmonic structures cannot be described by any analytical approach (which happens very often), then numerical calculations represent a powerful tool to determine the response of structures of different dimensions and shapes. One of numerical methods for solving Maxwell's equations is the Finite-Difference Time-Domain (FDTD) method.

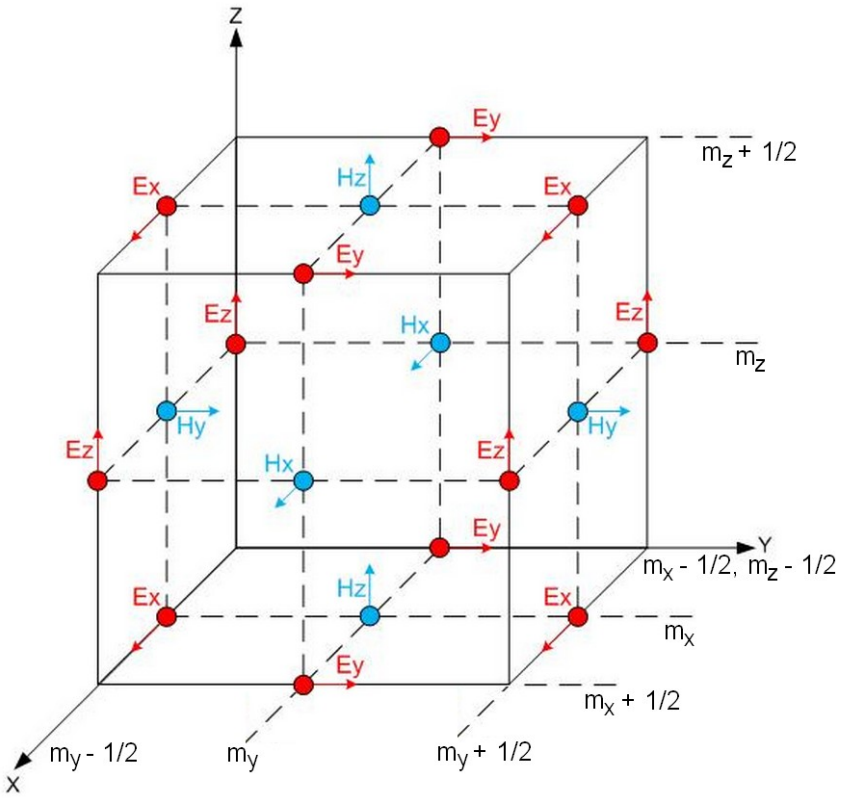

Figure 3.1: A visualization of usual 3D Yee cell of spatial indices (m_x, m_y, m_z). Magnetic components of the field are computed at the centre of cell faces, electric components at the centre of cell edges. Taken from [10]. It is also possible (but unusual) to calculate the magnetic components at the centre of edges and the electric components at the centre of faces; the FDTD method then works in the same way [11].

The FDTD method is based on a temporal and spatial discretization of following two curl Maxwell's equations (i.e. on the replacement of the derivatives by finite differences) and an electric field material equation for a non-magnetic medium:

$$\frac{\partial \vec{D}}{\partial t} = \nabla \times \vec{H}, \tag{3.1}$$

$$\frac{\partial \vec{H}}{\partial t} = -\frac{1}{\mu_0} \nabla \times \vec{E}, \tag{3.2}$$

$$\vec{D}(\omega) = \varepsilon_0 \varepsilon_r(\omega) \vec{E}(\omega). \tag{3.3}$$

The space is discretized using an ensemble of block shape cells, known as Yee cells [12]. One of them is shown in Figure 3.1. The block shape of cells, together with the spatial and temporal interleaving of cell points, where electric- and magnetic field is calculated (see Figure 3.1), ensure that conditions given by other two divergence Maxwell's equations are implicitly met [13].

As FDTD belongs to time-domain methods, performing the Fourier transform during or after the calculations enables to obtain the solutions of the equations also in frequency or wavelength domain. Therefore, with FDTD method one can also calculate a full range of useful quantities as a normalized reflection or transmission, a complex Poynting vector and a far-field projections.

3.1.1 Lumerical FDTD Solutions package

All the simulations in the presented thesis were performed with Lumerical FDTD Solutions software, which utilizes the FDTD numerical method for the solution of Maxwell's equations in non-magnetic media. It is capable to analyze the interaction of UV, visible, and IR radiation with complicated structures employing wavelength scale features [14].

3.2 Electron beam lithography

We used several material as a substrate; silicon (Si), nanocrystalline diamond (NCD) film on fused silica (SiO_2) and calcium fluoride (CaF_2). Substrates were pre-baked on a hot plate on 180 °C. We used 4% solution of polymethyl methacrylate (PMMA) in anisole as a lithographic resist. The relative molecular weight of used PMMA was $4.95 \cdot 10^5$. The bad resist adhesion to CaF_2 substrates was improved by spin-coating (2000 rpm for 30 s) of MCC Primer 80/20 prior to PMMA. The spin-coating of the resist on substrate was realized using Laurell 400 spin-coating device. The parameters of the spin-coating were 4000 rpm for 30 s for Si and NCD substrates, and 2000 rpm for 30 s for CaF_2. The presence of coated thin film changed the visual appearance of Si and NCD substrates, therefore, the naked eye inspection was sufficient to confirm the successful coating. However in case of transparent substrates like CaF_2, no change of an appearance is usually observed. Thus, we used a reflectometric technique to confirm the presence of the resist. Coated substrates were baked again on 180 °C for 90 s to harden the resist film. To prevent charging of non-conductive substrates (CaF_2) during the EBL the resist were covered by a thin film of conductive polymer Espacer 300z (2000 rpm for 30 s).

During the EBL, substrates were exposed to 30 keV electron beam in a conventional scanning electron microscope (SEM) Tescan Vega2 or Tescan Lyra3. After a series of test, the optimal electron dosage was determined to 265 μC/cm^2. Exposed samples were developed for 90 s in a mixture of methyl isobutyl ketone (MIBK) and isopropanol (IPA) in 1:3 ratio followed by rinsing in pure IPA for 30 s and demineralized (DeMi) water for 60 s.

In the next step, developed samples were metallized. We used an ion beam assisted deposition (IBAD) to deposit 3nm-thick film of titanium and 60nm-thick gold film. Metallized samples were put into a beaker with acetone and left overnight for a lift-off process. On the next day, the samples were rinsed by acetone, IPA and DeMi water from wash bottles. In several cases, an ultrasonic bath was also applied to improve the resist stripping.

3.3 Fourier transform infrared spectroscopy

The Fourier transform infrared spectroscopy has become a widely used technique for rapid microscopic analysis with the accuracy and sensitivity impossible to achieve by classic wavelength dispersive spectrometers [15]. A conventional dispersive method is based on dispersion of the incident light on a prism or grating. The energy of the incident radiation is varied over a desired range and a response is plotted as a function of frequency of the incoming radiation.

In Fourier transform spectroscopy, Michelson interferometer with a suitable beamsplitter (made of potassium bromide (KBr) for near- and mid-IR spectral regions) is usually employed and the sample is exposed to a short pulse of incoming radiation (for near- and mid-IR range usually coming from a heated silicon carbide bar usually called Globar which contains all the frequencies from particular range of interest. Therefore, one can get an optical response at a wide range of frequencies simultaneously. The frequencies can range from the ultraviolet to far infrared even using the same instrument, changing only the beam splitter in the interferometer and the detector. No traditional dispersive technique is capable of such wide frequency range.

4 Influence of NCD film on resonant properties of antennas

LSPR depends on the optical properties of the surrounding medium. This makes plasmonic structures (like antennas) suitable for sensing applications. By combining both, an NCD film as a substrate and a plasmonic antenna as a sensor, we can gain a biosensor based on LSPR. However, it is necessary to investigate the influence of NCD film on resonant properties (resonant wavelength, scattering cross section, local field enhancement) of plasmonic antennas first. Therefore this chapter deals with this investigation.

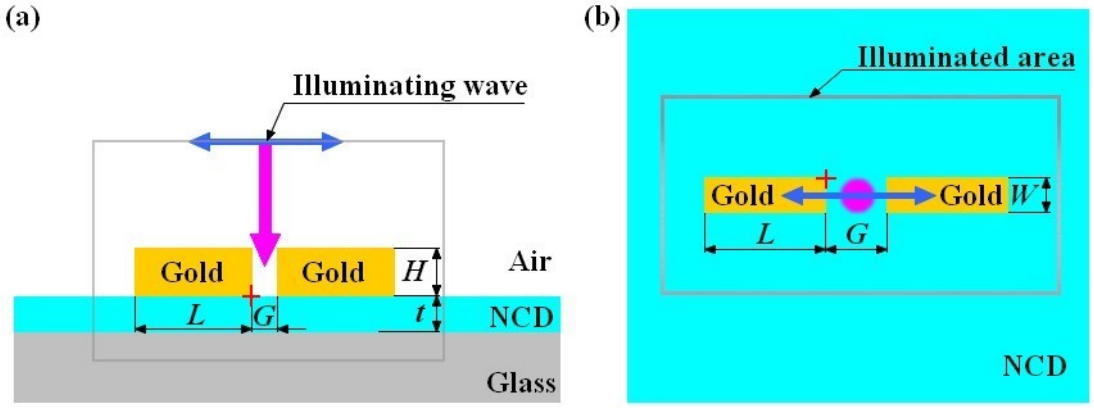

Figure 4.1: (a) Schematic side-view and (b) top-view of simulated (Lumerical FDTD Solutions) dimer antenna situated on NCD film of thickness t. Gold antenna rods of length L, width W and height H are separated by gap G. The purple arrow shows the direction of propagation of the illuminating light wave and the blue one shows the direction of light polarization. The red cross marks the place, where the maximum value of the local field enhancement is recorded.

Author of this thesis performed series of numerical calculations in Lumerical FDTD package [14] to evaluate resonant properties of gold dimer and single antennas situated on a glass substrate coated with an NCD film and compared to the results with the case without NCD. In addition, the antennas were optionally surrounded by NCD segments, the shapes, dimensions and positions of which is described below in proper sections. A scheme of the simulation geometry for a dimer antenna is shown in Figure 4.1.

4.1 Influence of antenna dimensions

Series of simulations were run for different dimensions of antennas. The length L of a single antenna (or a single antenna rod in case of dimer) was varied from 60 to 200 nm, width W and height H were varied from 20 to 100 nm. To investigate the influence of antenna dimensions on its resonant properties for all simulations in the series, the thickness of NCD film (when present) was fixed at 60 nm and the gap between the rods of dimer antenna was fixed at 40 nm. When length varied, the width and height of the antenna was fixed at 60 nm. When width or height varied, the length was fixed at 130 nm

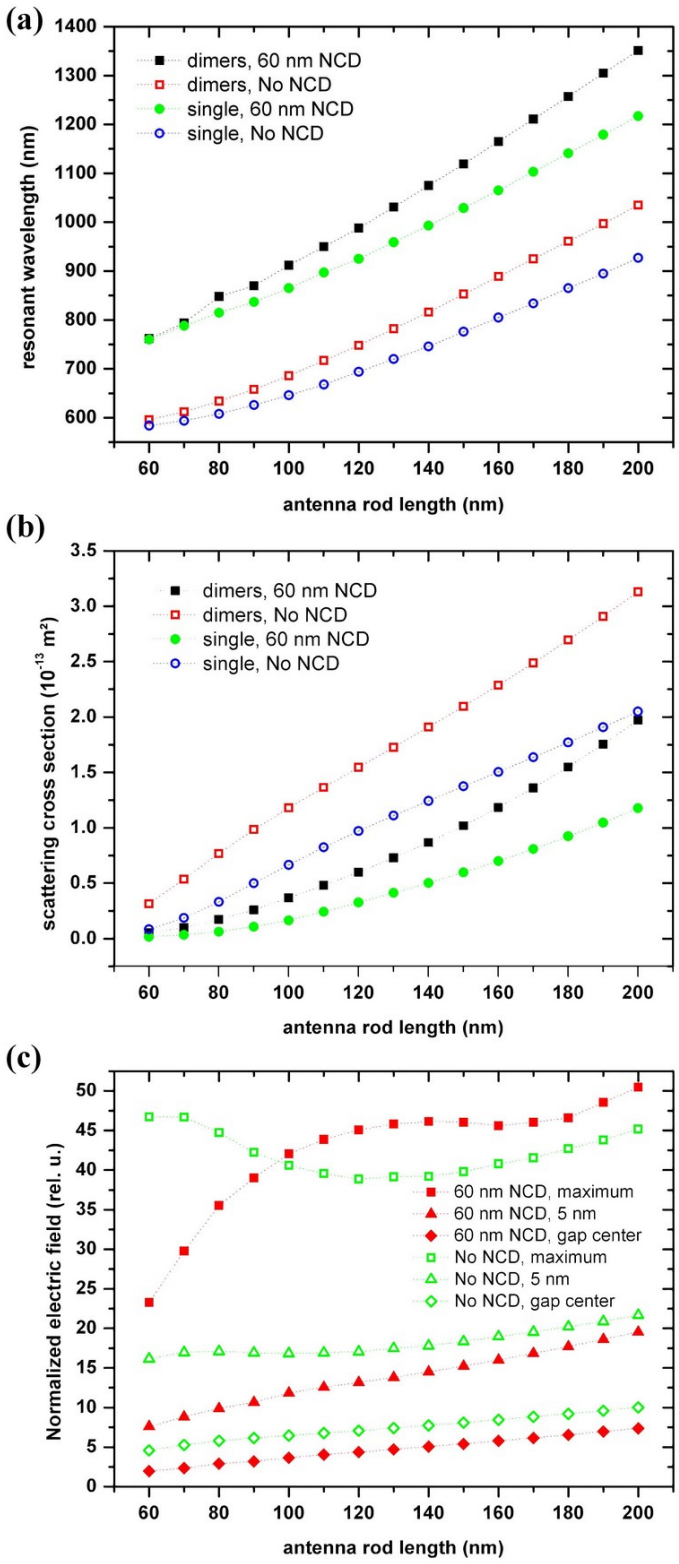

Figure 4.2: (a) Calculated wavelength of LSPR, (b) resonant scattering cross section, (c) resonant local field enhancement for several lengths of gold plasmonic antennas situated on a bare glass substrate and on a glass substrate covered by 60 nm-thick film of NCD. Antennas widths and heights were fixed at 60 nm and the gap between rods of dimer was 40 nm. The field enhancement was recorded at the vertices of the dimer antenna rods, 5 nm from the vertex towards the centre of the gap and in the gap centre.

and the remaining dimension was set to 60 nm. The antennas were illuminated from the top under the normal incidence by white light continuous wave in spectral range from 500 to 1600 nm using Lumerical Total-Field Scattered-Field light source.

The investigated features were the localized surface plasmonic resonant (LSPR) wavelength, scattering cross section and local near-field enhancement upon the antenna resonance in the close vicinity of the antenna. The spectral response of the antenna (LSPR wavelength and scattering cross section) to the incoming light was recorded by a set of six plane monitors placed all around the antenna outside the area illuminated by TFSF light source. The local near-field enhancement was recorded by monitors placed in the close vicinity of antenna walls and the antenna-NCD interface. As a measure of the electric field enhancement upon antenna resonance we used the maximum of local electric field in the vicinity of the antenna normalized to the incident field.

Results of the simulations with various length of antennas are summarized in Figure 4.2. As can be seen from Figure 4.2a, where the resonant wavelengths of gold plasmonic dimer and single antennas is shown as a function of antenna length, the resonant wavelength of antennas is linearly scaled with its length. This is not surprising, as all the theoretical approaches for the determination of the localized surface plasmon resonance wavelength (Eqs. (2.1), and (2.4)) expect this linear scaling with the antenna length.

Also the differences between the LSPR wavelength of antennas situated on glass and NCD film can be easily explained by the aforementioned models. Antennas are sensitive to the refractive index of their surroundings, which means that in the presence of the material of higher index, the resonant wavelength shifts to higher wavelengths. Therefore, the resonant wavelength of antennas on NCD film is red-shifted with respect to the antennas on bare glass.

The last feature noticeable in Fig. 4.2a is a difference of LSPR wavelength between the single and dimer antennas of same length and substrate. It is known from the literature (e.g. [16]) that when antennas are placed close to each other their plasmon modes hybridize and their resonant wavelength shifts. The dimer antenna consist of two rods and under the illumination the identical electric dipole emerges in both of them. When the distance between the rods is small enough, the dipoles interact with each other which leads to the shift of the dimer antenna resonant wavelength. Depending on the polarization of excited mode, the resonant wavelength is either red-shifted for longitudinal modes of blue-shifted for transversal modes [7, p. 82]. As the modes excited in the dimer antennas are longitudinal with respect to the orientation of antenna rods, the resonant wavelength is red-shifted.

The scattering cross section of the antenna also scales linearly with its length, as can be seen from Figure 4.2b. Naturally, dimer antennas scatter more light than single ones, because there are two antenna rods in dimer antenna instead of one. In comparison to single antenna, the geometrical cross section of the dimer antenna is double. But with the exception of the smallest antennas, the scattering cross section of dimer antennas is lower than double value of the scattering cross section of single counterparts.

The scattering cross section of antennas situated on NCD film is significantly lower then the cross section of the antennas of the same length on glass substrate. The relation for scattering cross section of a sphere (Eq. 2.3) can now serve us for the explanation of this

feature[1]. According to this equation, the value of the antenna scattering cross section is governed by the second power of its polarizability α and the fourth power of wavelength λ, which in equation (2.3) is hidden in the wavenumber k. As was discussed in foregoing text, the presence of NCD film below the antennas shifts their resonant wavelength to higher values. It can be seen from Figure 4.2a that the resonant wavelength of antennas on NCD is approximately 30 % bigger than for corresponding counterpart on bare glass substrate ($\lambda_{\mathrm{r,NCD}}/\lambda_{\mathrm{r,glass}} \approx 1.3$). The fourth power of this ratio yields $1.3^4 \doteq 2.86$. Therefore, due to the shift of the resonant wavelength, the scattering cross section of antennas on NCD film should be 2.86 times smaller than the cross section of their counterparts on bare glass substrate. The recorded data shows that this ratio of scattering cross sections varies between 1.66 for the largest antennas and 5.42 for the smallest ones. The deviation from calculated ratio 2.86 is caused by a different geometry and also by the change of the antenna polarizability α.

The maximum value of local field enhancement was recorded at the antenna vertex on the interface between air, antenna and substrate (in Figure 4.1 marked by red cross). The field enhancement was also recorded at the point situated 5 nm from the antenna vertex in the direction towards the gap centre and in the centre of the gap. The differences in the values of field enhancement between the antennas on NCD and glass counterparts can be seen from Figure 4.2c. To explain the differences, we will use the relation for the expression of electric near-field around the spherical particle

$$\vec{E} = \frac{\varepsilon - \varepsilon_{\mathrm{m}}}{\varepsilon + 2\varepsilon_{\mathrm{m}}} a^3 [3\vec{n}(\vec{n} \cdot \vec{E}_0) - \vec{E}_0] \frac{1}{r^3}. \tag{4.1}$$

It can be seen from this equation, that the electric near-field is given by the value of fraction $(\varepsilon - \varepsilon_{\mathrm{m}})/(\varepsilon + 2\varepsilon_{\mathrm{m}})$. In the spectral region under consideration, ε_{m} is almost constant ($\varepsilon_{\mathrm{m,glass}} \approx 2.14$, $\varepsilon_{\mathrm{m,NCD}} \approx 5.24$), but the dielectric function of gold varies significantly with wavelength. Therefore, the main reason for differences of field enhancement is the variability of gold dielectric function with wavelength. The difference in substrate dielectric function (when glass is replaced by NCD) causes the slight change of the wavelength, for which the Fröhlich condition (Eq. 2.2) is satisfied.

It can be seen from Figure 4.2c that for antennas on NCD film which are shorter than 100 nm, the maximum of the field enhancement is smaller compared with the corresponding counterparts on glass substrate. For longer antennas the maximum of the field enhancement is slightly bigger than for the antennas on glass. Nevertheless, when field enhancement is recorded further away from the antenna vertex, the values for antennas on NCD are always smaller then for antennas on glass. This means that the field is more confined to the antenna-air-NCD interface than to antenna-air-glass.

4.2 Influence of NCD film thickness

To determine the influence of the NCD film thickness on resonant properties of plasmonic antennas, another series of simulations were designed. In this series the length of antenna

[1]We expect that this feature is qualitatively shape independent, i.e. the results we would get for spherical particles of similar dimension might differ in the absolute values, but the observed trend in the data would be similar.

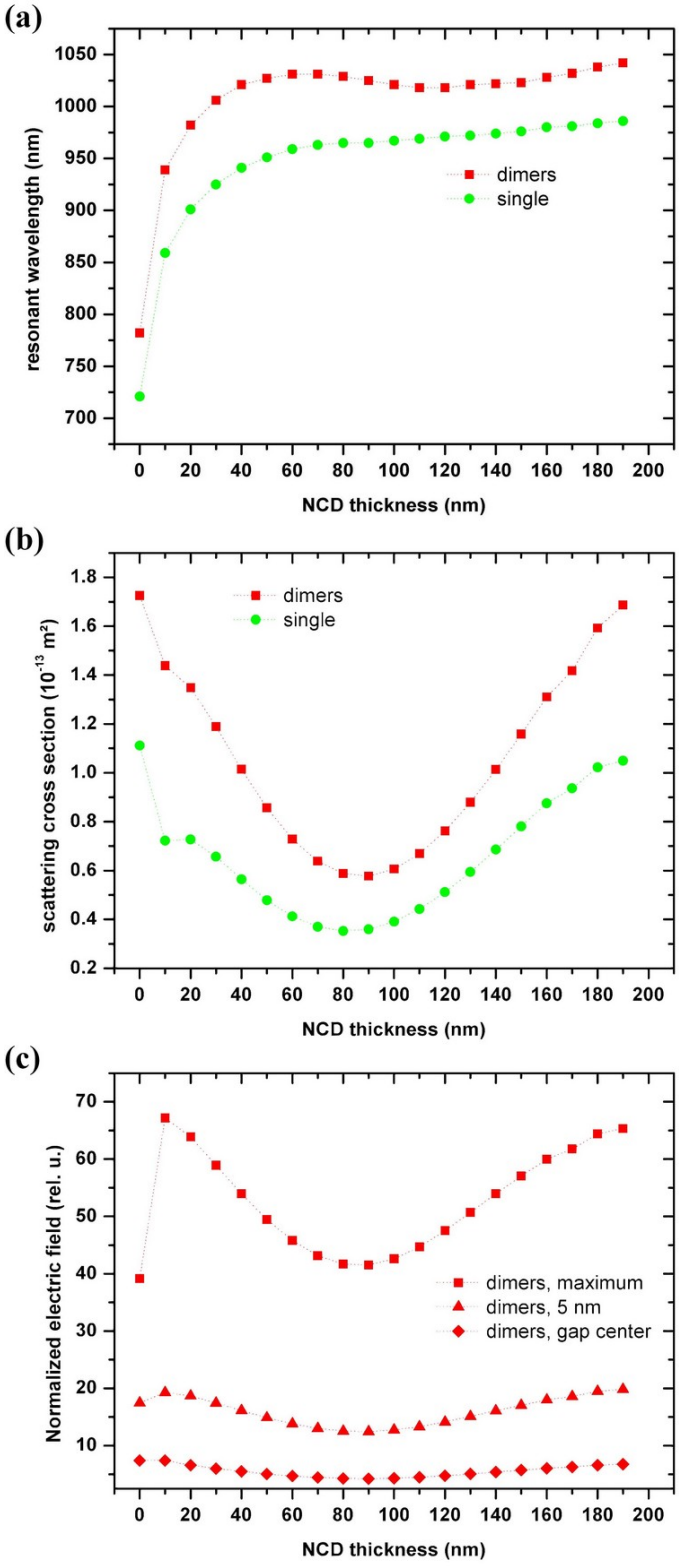

Figure 4.3: (a) Calculated wavelength of LSPR, (b) resonant scattering cross section and (c) resonant local field enhancement of single and dimer gold plasmonic antenna (dimensions 130 × 60 × 60 nm^3, gap between rods of dimer 40 nm) situated on a glass substrate covered by NCD film of various thickness. The field enhancement was recorded at the vertices of the antenna rods, 5 nm from the vertex towards the centre of the gap and in the gap centre.

was fixed at 130 nm, width and height at 60 nm and gap between antenna rods of dimer was 40 nm. The thickness of the NCD film between the antenna and glass substrate varied from 10 to 190 nm. The results of the simulations are summarized in Figure 4.3. It can be seen from this figure that the presence of an NCD film as thin as 10 nm on a glass substrate causes huge red-shift (approximately 150 nm) of the antenna resonant wavelength. With further growth of NCD film, the resonant wavelength is further red-shifted, but the rate of the red-shift gradually decreases with film thickness.

In Figure 4.3b one can see that the resonant scattering cross section of the antennas varies greatly with the thickness of NCD film and reaches its minimum for range of NCD thicknesses 80–90 nm. The drop in cross section is present for both single antennas and dimers. The values of cross sections in the minimum are only about one third of the maximum values. Similar drop also occurs for the resonant field enhancement (Figure 4.3c). From Figure 4.3a, we can see that for NCD film thicknesses bigger than 60 nm the resonant wavelength varies only slightly. Therefore, dielectric functions of gold and NCD do not significantly change with the NCD film thickness and such drop in scattering cross section (see Eq. (2.3)) cannot be explained neither by the change of antenna polarizability α nor by the pronounced change of resonant wavenumber $k = 2\pi/\lambda$. Therefore, this feature is the most probably connected with the thickness of the NCD film.

4.3 Influence of mutual position of NCD and antenna

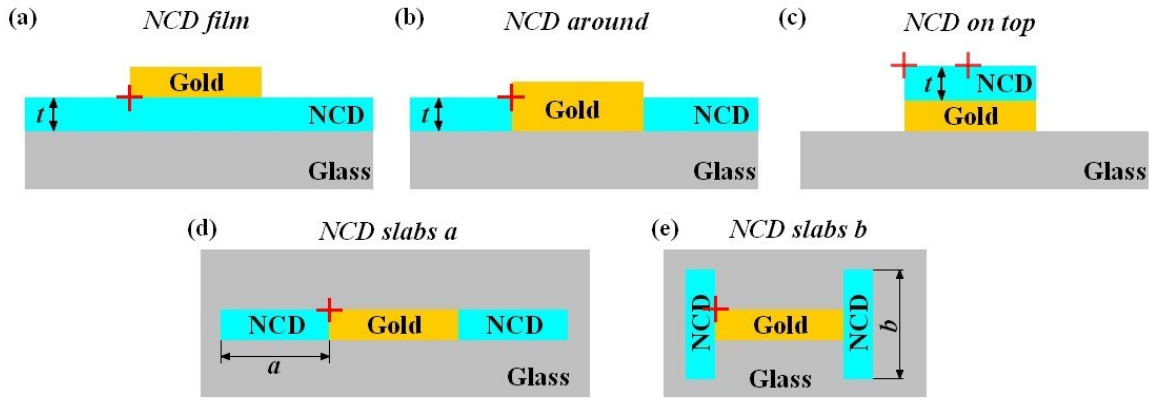

Figure 4.4: (a)–(c) Schematic side-view of simulation designs with different mutual position of NCD film of thickness t and antenna. (d), (e) Schematic top-view of simulation designs of single antenna with two types of NCD slabs placed at the antenna forehead. Red crosses mark the points, where the electric near-field enhancement was recorded.

The next series of simulations studied how resonant properties of the antennas vary with the mutual position of the antenna and NCD film or elements. Three different configurations, shown in Figure 4.4a–c, were studied. The dimensions of the antenna were fixed (length 130 nm, width and height 60 nm) and the thickness of the NCD film varied from 10 to 140 nm.

As NCD thin film could be used to accommodate organic species on its surface which presence would be sensed by plasmonic structures, the near-field enhancement at the air-

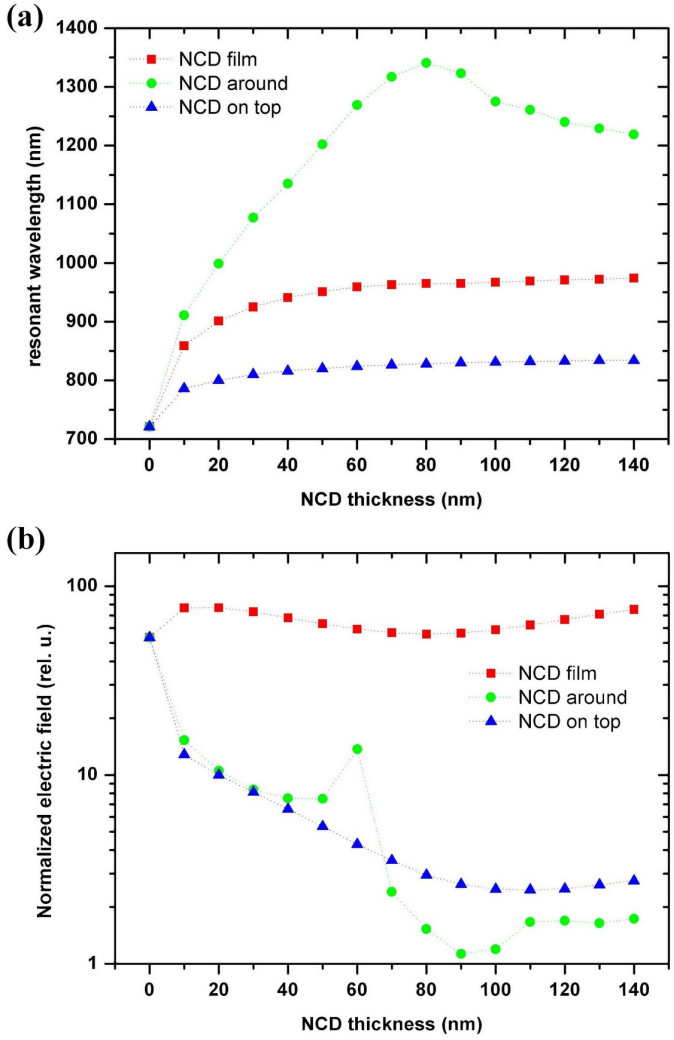

Figure 4.5: (a) Wavelength of LSPR and (b) resonant local field enhancement of single gold plasmonic antenna (dimensions $130 \times 60 \times 60\,\mathrm{nm}^3$) on or in NCD as shown in Figure 4.4a–c.

NCD interface in the close vicinity of the resonant antenna was the subject of our interest. This means that for the setup with the NCD film between the glass substrate and the single gold antenna (Figure 4.4a) the field enhancement was monitored near the base of the antenna. When the NCD film was located around the antenna (Figure 4.4b), the electric field was recorded at the interface between the antenna, NCD film and air. When a segment of NCD was placed only on the top of the antenna (Figure 4.4c), the field enhancement was monitored on the top of the NCD segment, above the antenna vertex (for thinner NCD segments) or above the centre of antenna (for thicker segments).

In Figure 4.5a, the evolution of the antenna resonant wavelength with increasing thickness of NCD is shown. From this figure it is apparent that the antenna sensitivity to the presence of NCD film significantly varies with the mutual position of the antenna and NCD. When no NCD is present, the resonant wavelength of the antenna is 722 nm. The antenna is the least sensitive to the presence of NCD segment on its top. In such case, the red-shift of resonant wavelength, caused by the presence of NCD segment, saturates for the 60nm thickness of the NCD segment at 830 nm. When NCD film is located between

the antenna and glass substrate, the sensitivity of the antenna is higher, i.e. the red-shift of the resonant wavelength with the thickness of NCD is bigger than in the previous case; the resonant wavelength reaches its maximum of 960 nm for the NCD thickness of 60 nm. Similarly to the previous case, no further red shift is observed for the NCD film thicknesses above 60 nm. We can assume that the antennas can sense[2] the presence of investigated material (e.g. organic species) at the distances comparable to the saturation of the resonant wavelength red-shift, i.e., 60 nm.

The sensitivity to the presence of NCD film is the strongest for the antenna laying directly on bare glass substrate (Figure 4.4b). The red-shift of the antenna resonant wavelength with increasing thickness of NCD film is biggest of all the investigated configurations. As the thickness of the film grows up to 80 nm, the corresponding average red-shift of resonant wavelength is approximately 70 nm for every 10 nm of NCD film thickness. For thicker films, the antenna resonant wavelength exhibits slight blueshift with the increasing thickness.

For sensing methods based on signal amplification by enhanced near-field, the quantification of this field enhancement becomes important. The maximum values of field enhancement in points of our interest (marked by red crosses in Figure 4.4) are shown in Figure 4.5b. When the antenna is placed on the glass substrate and either surrounded by NCD film or covered by NCD segment from the top (Figure 4.4b,c), the point of interest moves with the thickness of NCD. The highest fields related to the LSPR occur at the upper and lower antenna interfaces and these fields drop rapidly with increasing distance from the antenna interface. Therefore, the highest values of the field enhancement are found at the absence of NCD or when the thickness of surrounding NCD film is the same as the thickness of the antenna. The former corresponds to the case, when the monitoring point is at the glass-air interface close to the base of the antenna (configuration in Figure 4.4b) or close to the top of the antenna (configuration in Figure 4.4c). The latter corresponds to the case, when the monitoring point is in the vicinity of upper antenna interface.

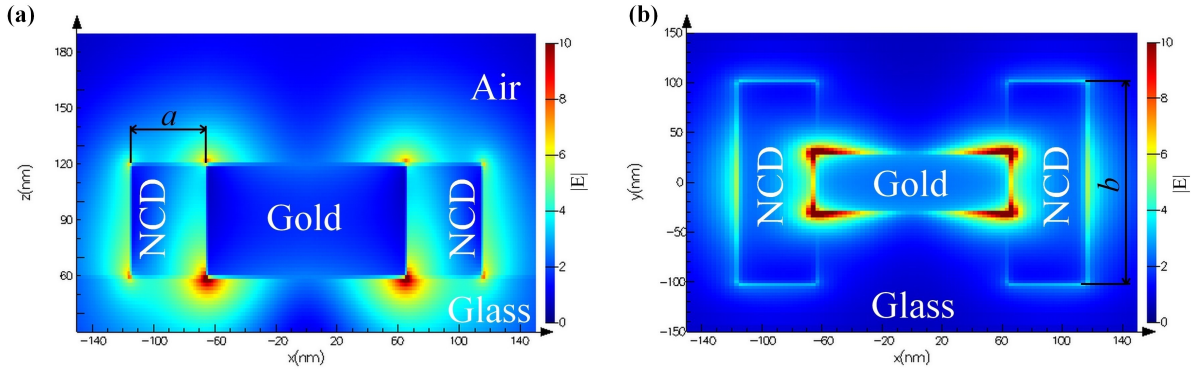

Figure 4.6: (a) Side- and (b) top-view of the calculated local field enhancement in the vicinity of a single gold antenna located on the glass substrate with *NCD slabs b* (Figure 4.4e). The antenna was excited by a plane wave (TFSF source) impinging from top and the magnitude of the electric field is expressed in units of the amplitude of the excitation field.

[2]The sensitivity of antennas will also be affected by the size of the surface area covered with the investigated material.

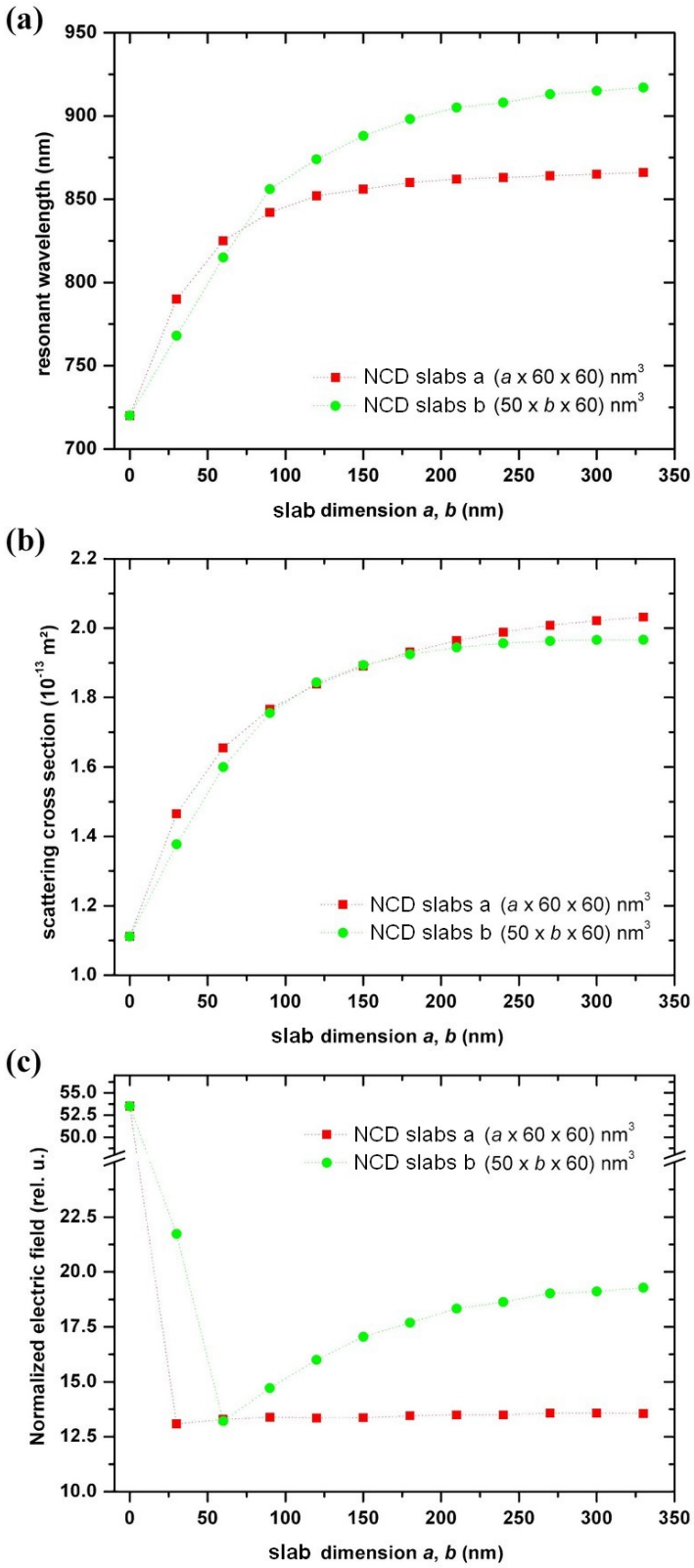

Figure 4.7: a) Wavelength of LSPR, (b) resonant scattering cross section and (c) resonant local field enhancement of single gold plasmonic antenna (dimensions $130 \times 60 \times 60\,\mathrm{nm}^3$) with NCD slabs at the antenna forehead (for geometry, see Figure 4.4d,e).

Spatially localized NCD slabs at the antenna foreheads

In the last series of simulations, two different types of NCD slabs were placed at the forehead of the antennas. One type, marked as *NCD slabs a* (Figure 4.4d), had the same width and height as the antenna (60 nm) and its length a varied in the direction parallel both to antenna longitudinal axis and polarization of the incident wave. The length b of the other type of slabs, marked as *NCD slabs b* (Figure 4.4e), varied in the direction perpendicular both to the antenna longitudinal axis and polarization of the incident wave. Width and height of these slabs were fixed at 50 and 60 nm, respectively.

A visualization of the resonant local near-field enhancement around the antenna with NCD slabs at its forehead is shown in Figure 4.6. As it can be seen from this figure, the electric field is not only enhanced in the vicinity of antenna interface, but also at the interface between the NCD slabs and air. From this point-of-view, it is possible to declare that the presence of the slabs increases the area around the antenna, where the electric field is enhanced.

The resonant wavelength of these antennas, scattering cross section and maximum field enhancement upon resonances shown as a function of varying dimensions of the slabs (a, b) can be seen in Figure 4.7. The red shift of the resonance wavelength (Figure 4.7a) due to growing dimensions of the slabs is in accordance with the higher index of refraction of NCD compared to the air and tends to saturate for the larger slab dimensions.

The scattering cross section significantly increases with both the dimensions of NCD slabs. The recorded increase of cross section is mainly attributed to the method of cross section calculation using the illumination of the antenna by TFSF source. The presence of NCD slabs near the antenna causes that another pair of scattering structures is present inside the space illuminated by TFSF radiation source (i.e. inside the space, where total field is calculated). Therefore, rather than the scattering cross section of a single gold antenna, the cross section in Figure 4.7b corresponds to a scattering cross section of a multi-structure system of a single gold and two NCD slabs.

4.4 Experiment

Due to limitations in both the fabrication and detection capabilities, we fabricated small series of single antenna arrays only. These served mainly to compare the resonant wavelength position with the results of simulations.

The author had been provided with several substrates of fused silica coated by a film of NCD. Thickness of the coating was 200 and 600 nm. Using spincoating, the substrate with 200 nm NCD film was covered by PMMA (4000 rpm, 30 s) and Espacer 300z (2000 rpm, 30 s). Then, arrays of gold plasmonic single antennas (array $50 \times 50\,\mu m^2$, antenna length $0.1 - 1.0\,\mu m$, spacing $0.5\,\mu m$ in both directions) were drawn into PMMA using Tescan Vega2 (30 keV, $275\,\mu C/cm^2$). The sample was then metallized (IBAD, 3 nm Ti, 60 nm Au). As the dimensions of the fabricated antennas were relatively small, no ultrasonic bath was applied during lift-off process.

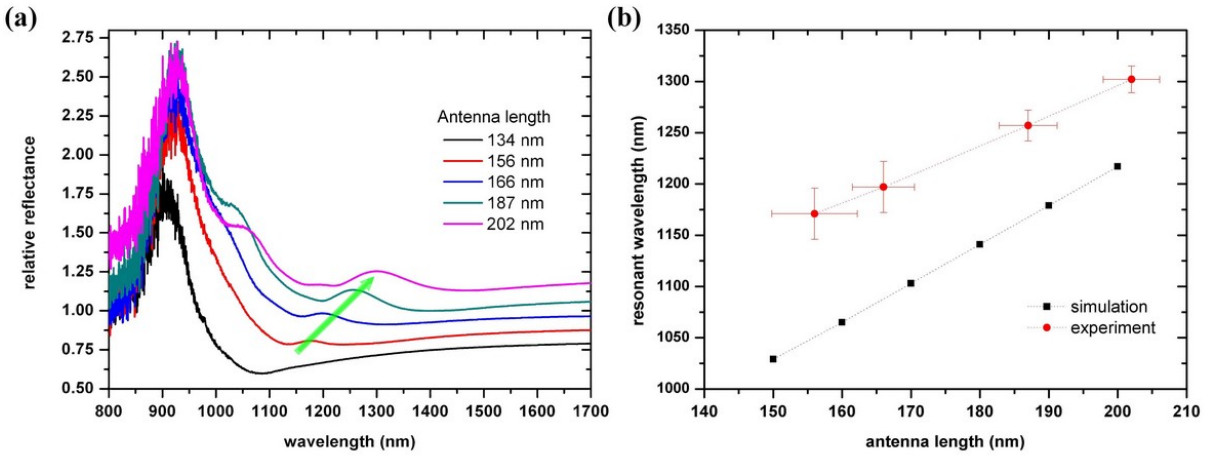

Figure 4.8: (a) Spectra of relative reflectance of gold plasmonic single antenna arrays of various antenna length fabricated by EBL on a fused silica substrate coated by 200 nm-thick film of NCD. The light green arrow shown the position of LSPR wavelength. Spectra were measured using microscopic FTIR (Bruker Vertex 80v + Hyperion 3000, InGaAs detector, CaF_2 beamsplitter). (b) Comparison of the experimental data with the results of FDTD simulations.

The measured FTIR reflectance spectra of fabricated antenna arrays are shown in Figure 4.8a. The green arrow in the figure indicates the shift of the resonant peak with the length of antennas in the array. The resonant wavelengths of antenna arrays are then compared (Figure 4.8b) with the results of simulations for single antenna of similar dimensions. As the dimensions of the antennas are small and the resonant peaks are weak and broad, the measurement uncertainty of both the antenna dimensions and resonant wavelength is relatively big. However, one can still see that the measured resonant wavelength of the antenna arrays is red-shifted by approximately 100 nm with respect to resonant wavelength of single counterparts. Such a large difference cannot be attributed to the limited accuracy of the calculations. As the spacing in both directions between the antennas in the array is 0.5 μm, which corresponds to approximately to half of the resonant wavelength, the red-shift is partly contributed by the mutual interactions of antennas in the array. Further, non-zero angle of incidence of illuminating light also contributes to the red-shift [17].

Another interesting feature of the reflectance spectra in Figure4.8a is the intense peak around 930 nm. Its position does not change with the length of the antennas, therefore this peak is not related to longitudinal LSPR.

Polarization properties of that peak can give us more information on its nature. Therefore, we put an NIR polarizer into the collection arm of the infrared microscope. In Figure 4.9 the resonant spectra of an antenna array (antenna length 187 nm) are shown for different polarization of the light reflected from the sample. When the light is polarized longitudinally, the LSPR peak is visible in the spectrum. The ratio between the peak at 930 nm and LSPR peak is significantly smaller then in the case when the light is not polarized. When the polarization is transverse, LSPR peak vanishes and the peak at 930 nm is higher and narrower. The peak at 930 nm is present for both longitudinal and transversal polarization. However, the intensity of reflected light at 930 nm is significantly higher for transverse (TE) polarization.

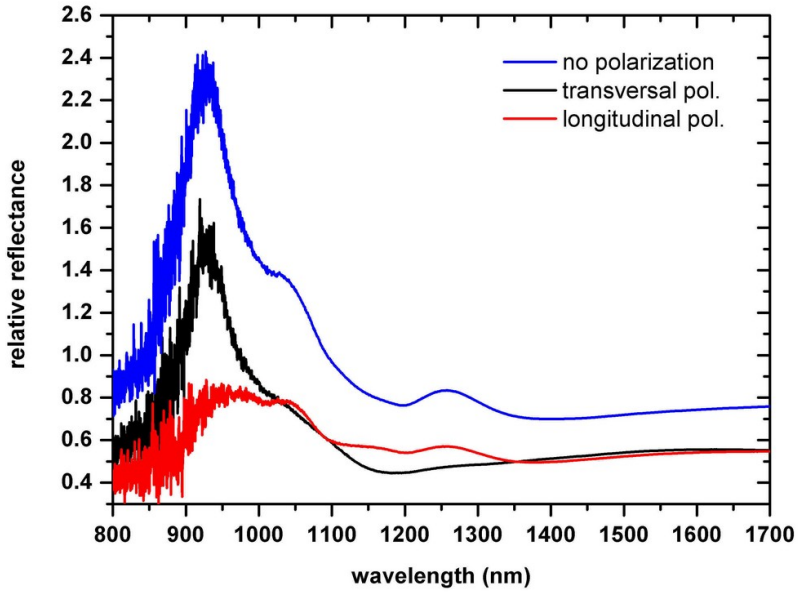

Figure 4.9: Relative reflectance spectra of antenna array (antenna length 187 nm) for different states of light polarization.

Now, it will be shown that the peak at 930 nm is caused by the light interference in the NCD film. The refractive index of NCD film is higher than the refractive index of air, therefore, the light reflected from this film is phase-shifted by π. This phase shift corresponds to optical path difference (OPD) $\delta_1 = \lambda/2$. Under normal angle of incidence, the light reflected from the interface NCD-glass has OPD

$$\delta_2 = 2n_{\mathrm{NCD}}t, \tag{4.2}$$

where $n_{\mathrm{NCD}} \approx 2.29$ is the real part of NCD refractive index and t is thickness of the film. In case of 200 nm-thick NCD film, $\delta_2 = 916$ nm. The light beams (the one reflected from air-NCD interface and the other from NCD-glass interface) interfere with each other. In case of interference minimum, the condition for the path difference Δ between the interfering light beams is following:

$$\Delta = \delta_2 - \delta_1 = (2m-1)\frac{\lambda}{2}, \tag{4.3}$$

where $m = 1, 2, 3, \ldots$ is the order of interference minimum. The solution of this equation yields

$$\lambda = \delta_2/m \tag{4.4}$$

$$\lambda = \delta_2 = 916\,\mathrm{nm}, \text{for } m = 1. \tag{4.5}$$

Therefore, for $\lambda = 916$ nm, the reflectance of the substrate reaches its minimum. The quantity measured by FTIR is a spectral response function of antennas which in reflection configuration of FTIR setup corresponds to relative reflectance R_{a} of antennas (which is shown in Figure 4.8a). To get this quantity, two measurements of the reflected light spectral intensity are taken by FTIR microspectrometer. One measurement is realized in

the part of the sample, where no antennas are situated (I_s), and the other is realized on the array of antennas (I_a). The resulting relative reflectance R_a is given by its ratio

$$R_\mathrm{a}(\lambda) = I_\mathrm{a}(\lambda)/I_\mathrm{s}(\lambda). \tag{4.6}$$

At $\lambda = 916\,\mathrm{nm}$ the reflectance of the substrate drops to its minimum; at this wavelength the intensity of reflected light reaches only 3 % of incident light intensity and the value of I_s can be consider as very small. On the other hand, the intensity of the reflected signal can be increased, when particles of a good reflector, like gold ones, are placed on the substrate surface. The gold antennas, which are sparsely[3] situated on the NCD film are clearly out of the resonance at $\lambda = 916\,\mathrm{nm}$. Nevertheless, the antennas act as simple mirrors and their presence increases the reflected signal I_a. And since, I_s is relatively small around $\lambda = 916\,\mathrm{nm}$, the value of relative reflectance R_a (Eq. 4.6) quite high around this wavelength.

In the experimental spectra of relative reflectance of antenna arrays (Figure 4.8a), we found a large peak at 930 nm and we explained its origin in the foregoing text. However, according to our theory, the peak position should be at 916 nm. This difference can be caused by a combination of several factors. First, the refractive index of NCD could be slightly higher (up to $n_\mathrm{NCD} = 2.32$). Second, the NCD film could be thicker. A change of NCD film thickness by 3 nm to 203 nm would shift the peak position to 930 nm. Last, but not least the influence of the angle of light incidence has to be mentioned.

In the theory, we operate with normal incidence of the light. However, the geometry of Cassegrain 36× objective, which we used in the measurements, prohibits the normal incidence of the light. Actually, the secondary mirror of the objective blocks the light which would hit the sample under the angle smaller then 10 ° [17]. Non-zero angle of incidence means that the OPD δ_2 is bigger than in our calculations and so has to be the wavelength, where the relative reflectance reaches its minimum. The angle of incidence 15° would result in the shift of the peak posiiton from 916 nm to 922 nm.

[3]The coverage goes from approximately 4 % for the smallest antennas to approximately 6 % for the biggest ones.

5 Functionalization of antennas for biosensing

A LSPR wavelength sensitivity to the changes of the refractive index of the surrounding medium makes plasmonic antennas ideal for sensing. The presence of a material around antennas results in changes of the effective refractive index and therefore in a shift of LSPR wavelength. To ensure that antennas will detect only the presence of the specific agents, samples with antennas have to go through the process of functionalization. In this process, the surface of antennas is modified by substances which bond to as a few other substances as possible, but which had a strong bond to an agent which presence should be detected. Ideal for the role of such mediator between antennas and detected agent are bio-molecules. Main advantage of bio-molecules usage is their highly-specific interaction (e.g. antigen-antibody interaction) and a possible tuning of molecular length and topology [18]. The main goal of our work in this field was to use the antennas to sense the presence of streptavidin in their vicinity.

5.1 Samples and methods

Author of this thesis fabricated several samples with arrays of gold plasmonic dimer antennas (length 0.6–2.0 μm, width 0.4 μm, height 0.06 μm, gap between the rods of dimers 0.2 μm) on Si(100) substrates by EBL. These samples were brought to Elettra synchrotron facility in Trieste, Italy, where they were functionalized (covalent binding technique, N:1 spatial mode) in cooperation with Nano-Innovation Laboratory of Dr. Loredana Casalis. The mid-IR optical response of functionalized antennas was measured at SISSI beamline with the assistance of Dr. Lisa Vaccari. The response was measured before and after each of the functionalization steps by micro-FTIR Bruker Vertex 70 connected with infrared microscope Hyperion 3000 using conventional reflection setup (Globar light source, Ge on KBr beamsplitter, LN_2 cooled MCT detector).

5.2 Functionalization process

At first, the samples were cleaned off any possible organic contamination in an oxygen plasma (75 % Ar, 25 % O_2, 120 s, 30 Pa). O_2 plasma treatment also made the surface of Si hydrophilic which is crucial for the successful functionalization. The functionalization process consisted of three major steps which are schematically shown in Figure 5.1. The first functionalization step was to bind thiolized 24-basis-single-strand (ss) DNA chains of coagulation factor 5 (CF5) from phosphate buffer saline (PBS) solution to gold antennas by the chemisorption of thiol molecules to gold. This covalent coupling of ligands to nanoparticles is a reliable and robust route to add both the function and chemical stability. After that, the CF5 strands which were bound to the gold by the physisorption (instead of intended chemisorption) were removed using a solution of ethylene-glycol-terminated alkylthiol (TOEG6).

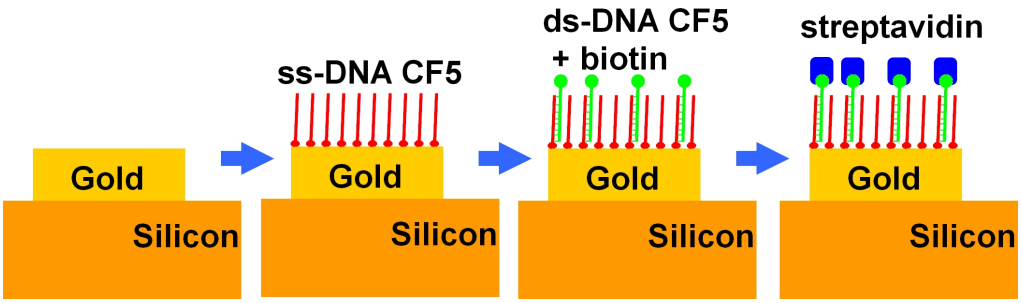

Figure 5.1: A simple scheme of functionalization steps. The first step is to bind thiolized 24-basis-single-strand (ss) DNA chains of the coagulation factor 5 (CF5), the second to hybridize the bound CF5 strands with a complementary CF5 ss-DNA basis with biotin molecules at the end of the chains and the final step was to bind streptavidin from an investigated solution to biotin molecules.

The second step was to hybridize the CF5 strand at the antennas by a complementary CF5 ss-DNA basis with biotin molecules at the end of its chains. Biotin binds strongly to streptavidin, therefore it mediates binding of streptavidin to antennas in the case of its presence in investigated solutions. The binding between biotin and streptavidin is the strongest known non-covalent and completely reversible bond [18]. The final step was to drop an ethanol solution with streptavidin over the antennas and rinse it by DeMi water after an hour.

5.3 Streptavidin detection

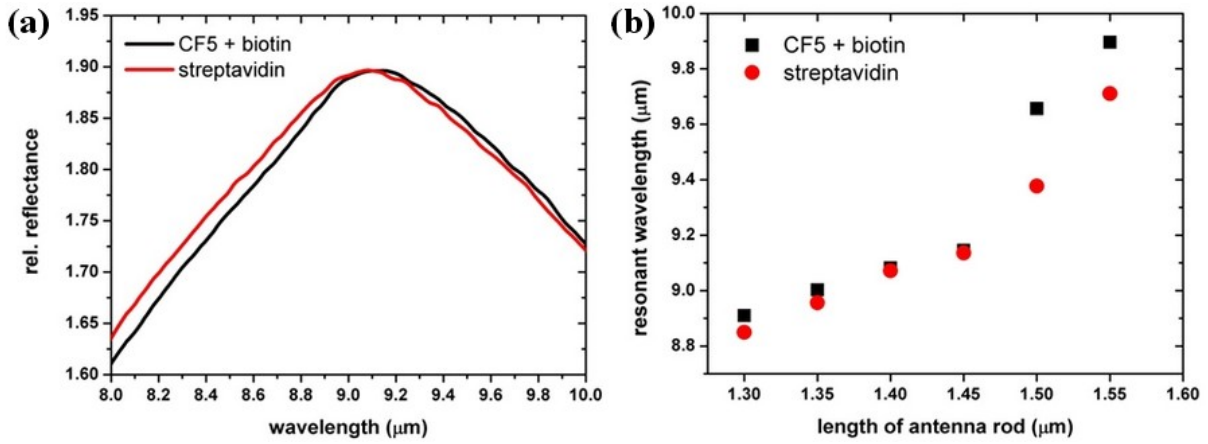

Figure 5.2: (a) Localized surface plasmon resonant peaks of a gold dimer antenna array (length of antenna rods 1.40 μm) functionalized by a double stranded DNA chain CF5 with the biotin molecule (black) and streptavidin bound to biotin (red), and (b) the wavelengths of the resonant peak maxima for the arrays of the rods with the length between 1.30 and 1.55 μm.

FTIR measurements (in reflection configuration only) were performed after each functionalization step. However, the most important was the difference in spectra which were taken before and after last step (i.e. without and with streptavidin). The slight shift in spectra measured before and after adding streptavidin on the sample (Figure 5.2) shows

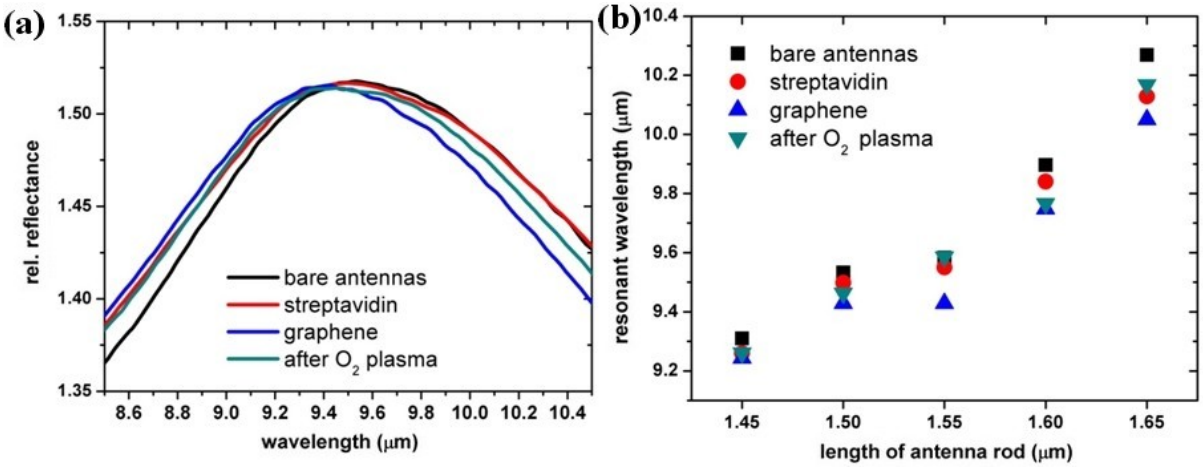

Figure 5.3: (a) Localized plasmon resonant peak of a gold dimer array of antenna rod with the length $L = 1.50\,\mu$m (black) and its shift caused by the presence of streptavidin at the antennas (red), by covering the antennas by a single layer of CVD graphene (blue) and after the removal of graphene and organics in oxygen plasma (turquoise), and (b) the wavelength of the resonant peak maxima for gold dimer antenna arrays with the rod length between 1.45 and 1.65 μm.

that we have successfully indirectly detected its presence. However, this spectral shift is relatively small in comparison with the results which were achieved in visible spectral region and presented, for example, in [19].

5.4 Influence of graphene layer

From the aforementioned results, we know that the antennas are capable to detect the presence of a single layer of self-assembly molecules on their surface. To find if the antennas are capable to sense the presence of a single atomic layer on their surface, we decided to cover the already functionalized antennas by a single layer of graphene.

The graphene was prepared (CVD) on a substrate of copper foil from CH_4/H_2 plasma of 22:13 sccm ratio, the pressure of approximately 10 Pa and the temperature of 1000 °C. Later, it was transferred from the copper foil on the sample with functionalized antennas. The Raman spectrum of this graphene layer (NT-MDT Ntegra Spectra, laser wavelength 532 nm) exhibited unique features confirming that it is indeed a single layer of graphene. FTIR measurements of relative reflectance of plasmonic antennas covered by this graphene single layer showed (Figure 5.3) shift of the resonance wavelength caused by the presence of graphene. After these measurements the samples were cleaned again in O_2 plasma which removed graphene and organics (DNAs, streptavidin, ...). The FTIR measurement of antenna resonant spectra taken after O_2 plasma cleaning showed a back-shift in antenna resonant wavelength. Despite that the shifts of resonant wavelength were relatively small, these measurements showed that the antenna arrays are capable to sense the presence of materials as thin as single atomic layer in the close vicinity of the antenna arrays.

6 Unidirectional antennas

As shown in [20] and [21], plasmonic antennas can serve for coupling the light into optical waveguides. Let us imagine a plasmonic antenna on top of an optical channel or rib waveguide. Refractive index of the waveguide has to be higher than the index of the bottom cladding and surrounding air serves as a side- and top-cladding. Plasmonic antennas preferentially scatter the incoming light in the medium of a higher refractive index [20]. Therefore, the light coming from air is partially *redirected* by the antennas into the waveguide. When illuminated under a normal angle of incidence, straight rod-like antennas scatter the same amount of light in both waveguide directions [22]. When specific configuration (e.g. Yagi-Uda) [20] or geometry (e.g. V-shape) [22] of rod-like antennas is used, the light scattering can be highly directional at specific wavelengths.

In this chapter, we will deal with the plasmonic V-shaped antennas. The V-shaped antenna (or shorter V-antenna) consists of two identical antenna rods of length L, width W and height H which enclose an angle 120 °. The geometry of the V-antenna is shown in Figure 6.1a.

In the theory of antennas, the figure-of-merit for an antenna is represented by antenna directivity D. There exist several definitions of this quantity [23, p. 44–56]. For our needs, we adopted the definition from [22], where the directivity D is defined by following

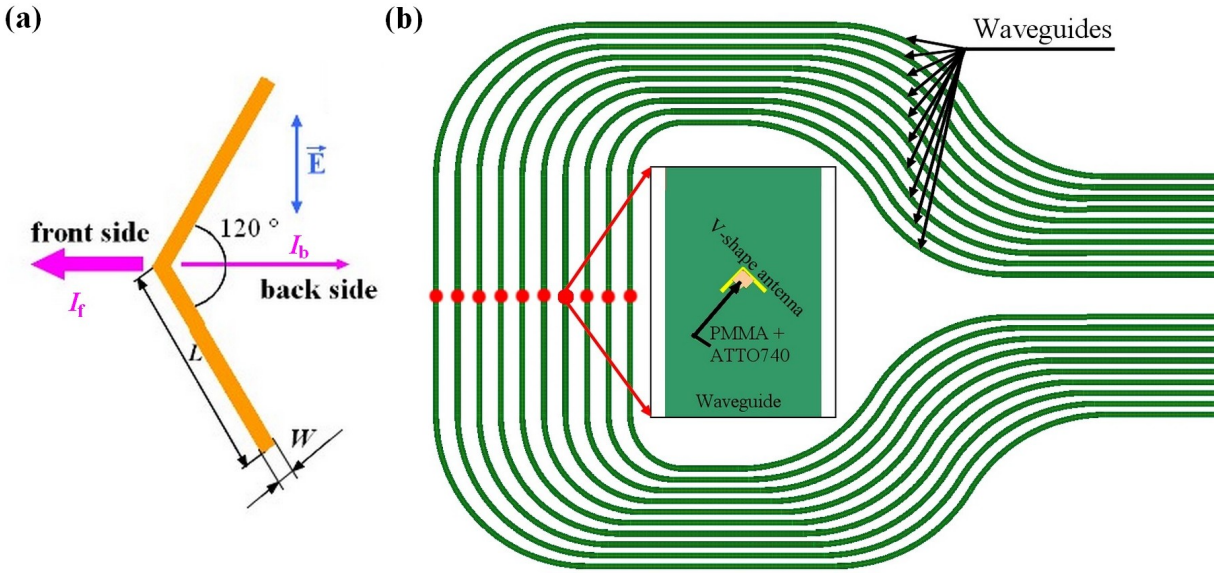

Figure 6.1: (a) Schematic top-view of V-shaped plasmonic antenna. The blue arrow shows the polarization of electric component of incoming electromagnetic wave. All the V-antennas which are presented in the thesis has inner angle between the antenna rods 120 °. According to [22], the directional effects of V-antennas are the biggest for this value of the inner angle. The region to the left of the antenna central vertices we labeled as *front side* and the region to the right as *back side*. (b) Part of the EBL mask with a set of channel waveguides as was designed in IMEC, Belgium. A single gold antenna (or an array of antennas up to 5 x 5) is situated on top of the waveguides in the mid of their length. A mixture of PMMA and ATTO740 dye is located in the antenna inner part. The red dots mark the places, where antennas are placed.

relation as a ratio between the light intensity scattered by V-shaped antenna into the front side (I_f) and back side (I_b):

$$D = 10 \log_{10} \frac{I_\mathrm{f}}{I_\mathrm{b}} \ [\mathrm{dB}]. \tag{6.1}$$

6.1 V-shaped antennas for visible and near-infrared region

During his internship in IMEC research institute in Leuven, Belgium, the author of this thesis joined the project of experimental evaluation of the directivity of V-shape antennas on silicon nitride waveguides. In figure 6.1b, one can see a scheme of antenna on silicon nitride waveguide as it was designed in IMEC.

The fabrication process was following. A silicon substrate with 2μm film of the thermally grown silicon dioxide and 180 nm of silicon nitride (Si_3N_4) was coated by a 10nm film of sputtered titanium and 50 nm of gold. The gold film was then coated by a film of ma-N 2403 negative resist. Using the EBL, a mask of V-shape antennas of the rod length L from 180 to 250 nm and the inner angle between rods of 120 ° was drawn into the coated resist film. After the development, the pattern of the mask was transferred to the gold film by Xe-ion milling, which removed all the gold, but the parts covered by the resist. Then, samples were coated by FOx-12, a hydrogen silsesquioxane (HSQ) based negative resist, and another EBL process was used to draw a mask of waveguides. After the development, the mask pattern was transferred to Si_3N_4 by SF_6/C_4H_8 inductive coupled plasma reactive ion etching (ICP/RIE) that removed all Si_3N_4 with the exception of parts covered by FOx-12. The last fabrication step was the coating of samples by a mixture of the PMMA positive resist and the ATTO740 fluorescent dye. After the EBL and the development, the PMMA with ATTO740 molecules was removed from Si_3N_4 waveguides and from the vicinity of antennas with the exception of specific area in the inner part of V-antenna (see Figure 6.1b).

For the measurements, the samples were diced to several pieces which were attached to the sample holder by a two-side duct-tape. For the illumination of antennas, Spectra physics Tsunami pulse laser at 730 nm was used. The light from the laser (optical power 700 mW, 80 MHz repetition rate) passed through a set of attenuators and was coupled to a multimode optical fiber. At the experimental setup, the laser light was outcoupled from the fiber and focused by 5× objective on a pinhole with the diameter of 5μm, which acted as a spatial filter. Light from the pinhole passed through 750 nm short-pass filter and was collimated and directed into the objective (Mitutoyo NIR 20×, NA 0.40), which focused the light on antennas located on the top of a single waveguide. The light (both laser light and fluorescence of ATTO740) was partially coupled by the antennas to the waveguide. The power of the light illuminating antennas was estimated to be in units of mW due to high losses in the excitation path.

A collection objective (Olympus UMplanFl 20×, NA 0.46) was focused on the edge of the sample part, collected the light coming out of the waveguides and directed it through 750 nm long-pass filter (to filter laser light from the detected signal) into an imaging

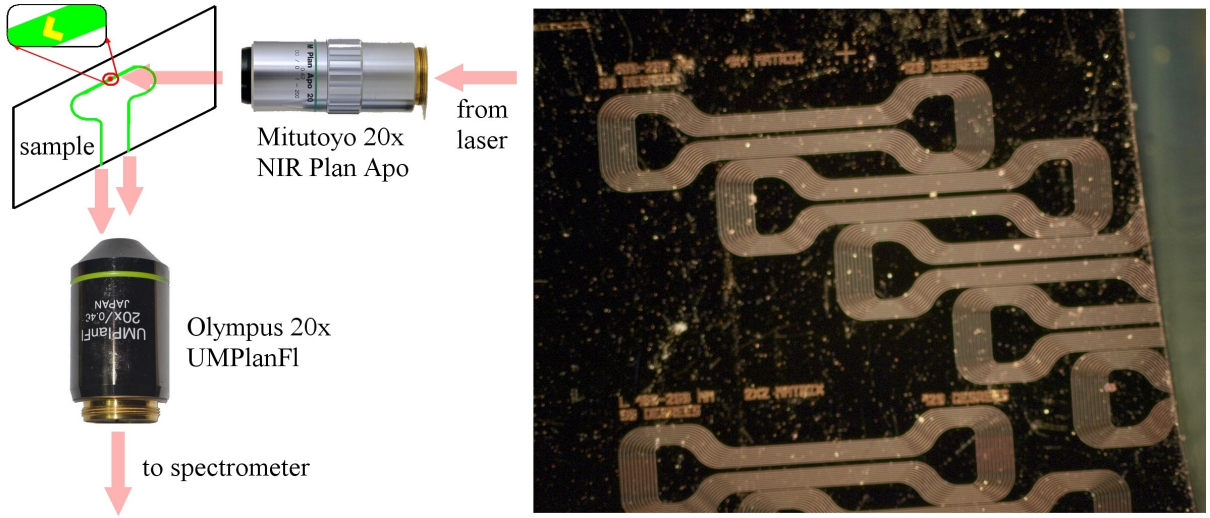

Figure 6.2: Schematic of an experimental optical setup (left) and a dark-field microscopic image of Si_3N_4 channel waveguides (right).

spectrograph (Newport MS260i). A simple schematic of experimental configuration is in Figure 6.2.

Measurements obtained during author's stay in IMEC show that V-shaped antennas successfully couple incident light as well as the light from emitters situated nearby the antennas into waveguides. Due to the low-symmetry of the antenna shape this coupling is directional with the directivity up to 7 dB (Figure 6.3) for the excitation laser but much smaller the fluorescence signal, where the directivity oscillates from 2 dB to −1 dB. Nevertheless, such low directivity has been reported for similar antennas by Vercruysse in [24].

6.2 Infrared V-shaped antennas

Due to the availability of IPE BUT fabrication and detection capabilities, further investigation of V-shaped antennas resonant properties were done in mid-infrared spectral region.

6.2.1 FDTD calculations

Series of numerical computations were run in Lumerical FDTD Solutions to determine the resonant properties of the V-shaped gold plasmonic antennas. To reduce the time complexity of the simulations, the model of free-standing antennas (no substrate) was used. As the simulations were done in mid-IR spectral region, where metals are good conductors and both Si and CaF_2 substrates have negligible absorption, it was then very easy to estimate the resonance of antenna on substrate from the results for free-standing antenna. The *nature* of this conversion consists in multiplication of the wavelength scale by substrate index of refraction. The resonant spectrum of free-standing gold V-antenna

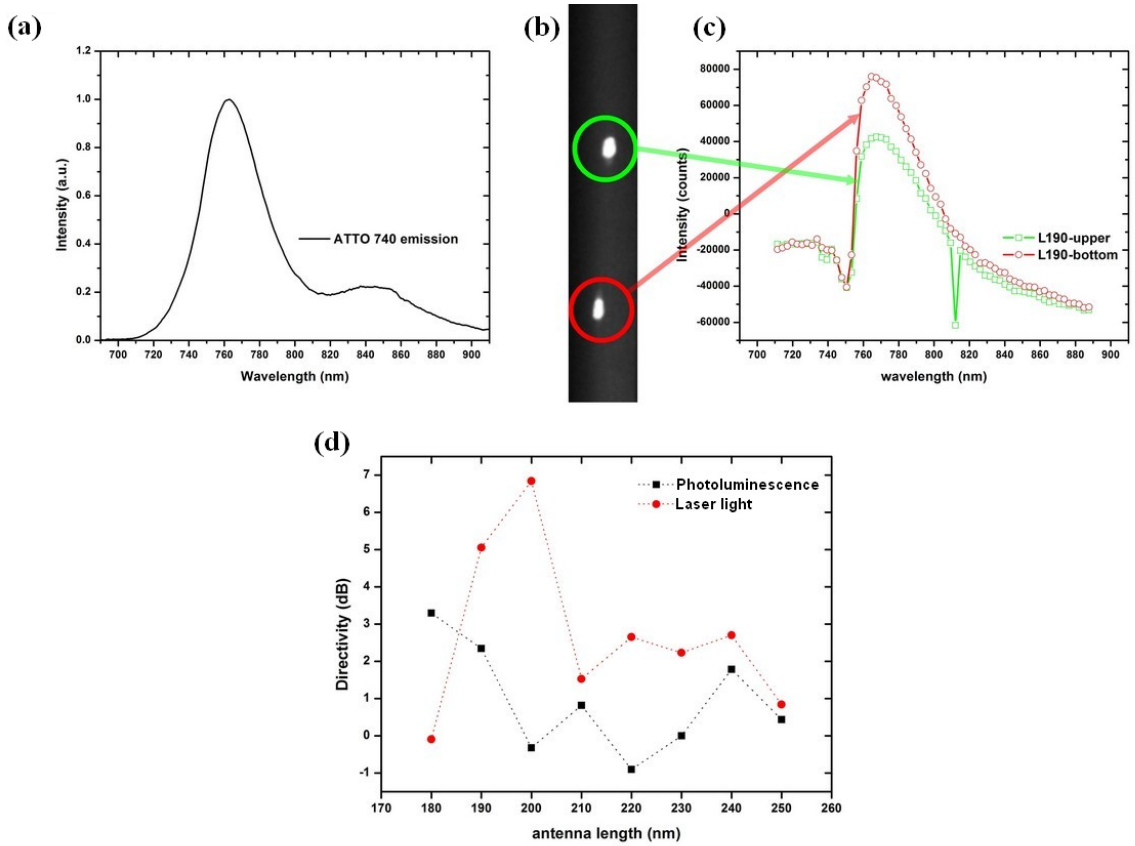

Figure 6.3: (a) Emission spectrum of the ATTO740 luminescent dye, (b) photoluminescent signal of ATTO740 as detected by a CCD camera of the spectrograph, (c) spectral analysis of the bright spots from (b) shoving emission from ATTO740 and long-pass filter cut-off wavelength at 750 nm, (d) directivity of antennas based on the ratio between the intensities of light coming out from both waveguide ends.

of length $L = 2.5\,\mu$m is shown in Figure 6.4. In this spectrum, peaks of both the dipole and quadrupole mode are clearly visible.

The dipole and quadrupole mode differ by charge distribution over the antenna and therefore, by the electric field in the antenna vicinity, as it can be seen in Figure 6.5a,b. These differences in antenna near-field also affect the antenna far-field. While the angular radiation pattern of dipole mode is almost the same for both scattering directions (Figure 6.5c,e), the pattern of quadrupole (Figure 6.5d,f) differs significantly. It seems that at the wavelength of the quadrupole mode the most of the incident light is scattered to the half-space in front of the antenna, while at the wavelength of dipole mode, the antenna scatters approximately the same amount of light in both half-spaces.

By integration of light intensity distribution (like those shown in Figure 6.5c–f) in both half-spaces for different wavelengths, we calculated the intensity of the light scattered by the V-shaped antenna in each of the half-space. Then, we used Equation (6.1) to calculate the antenna directivity D. In Table 6.1, there is shown calculated directivities for the wavelengths of the dipole mode, the quadrupole mode, and the wavelength at which the directivity reaches its maximum.

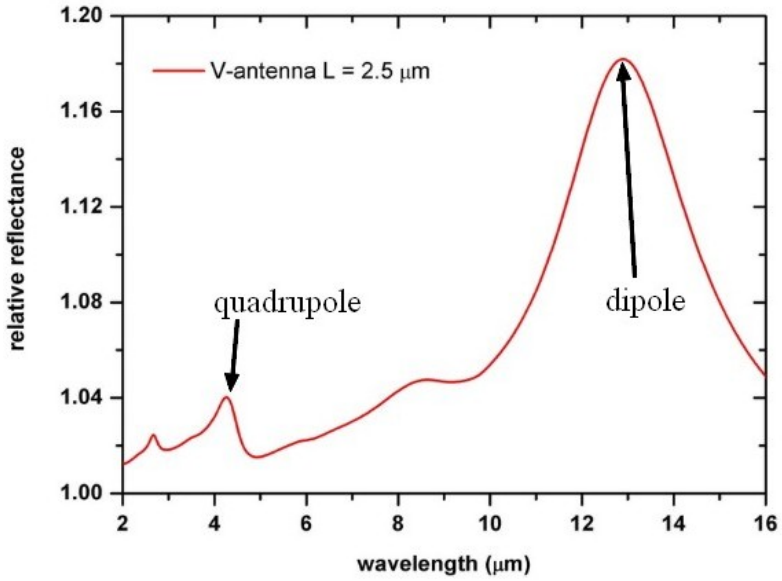

Figure 6.4: Calculated resonant spectrum of free-standing V-shaped antenna ($L = 2.50\,\mu$m, $W = H = 50\,$nm).

Table 6.1: Wavelength of modes and directivity of free-standing V-antenna ($L = 2.5\,\mu$m, $W = 0.05\,\mu$m, $H = 0.05\,\mu$m).

	dipole mode	quadrupole mode	maximum of directivity
wavelength (μm)	12.89	4.25	4.45
directivity (dB)	0.19	4.88	9.45

6.2.2 Experiments

Series of V-shaped gold plasmonic antenna arrays ($100 \times 100\,\mu$m^2) were fabricated by EBL on substrates of Si(100) and CaF_2. Due to the limitation of our fabrication capabilities, the width of the antennas was set to $W = 0.4\,\mu$m.

The mid-IR optical response of fabricated V-antenna arrays was measured by micro-FTIR (Bruker Vertex 80v + Hyperion 3000) in conventional reflection setup (Globar source of unpolarized IR radiation, Ge on KBr beamsplitter, MCT detector). The experimental resonant spectra of gold V-antennas on Si substrate are shown in Figure 6.6. In this figure, the red-shift of resonant wavelength with increasing arm length is indicated by arrows for both for dipole and quadrupole mode. As the width of the antennas is quite large, transverse *width* resonant mode is also visible in spectra. The intensity of the quadrupole-mode signal is very weak, this is especially apparent for antenna of length $1.3\,\mu$m, where the intensity of dipole and quadrupole peak can be directly compared.

The weak signal from quadrupole mode of antenna on silicon substrate is mainly caused by high reflectance of silicon substrate. Due to its high refractive index ($n \approx 3.42$ in mid-IR) silicon is relatively good reflector. Therefore, the presence of gold antennas on its surface enhance the reflectance only marginally. The solution of this issue consists in the change of the substrate.

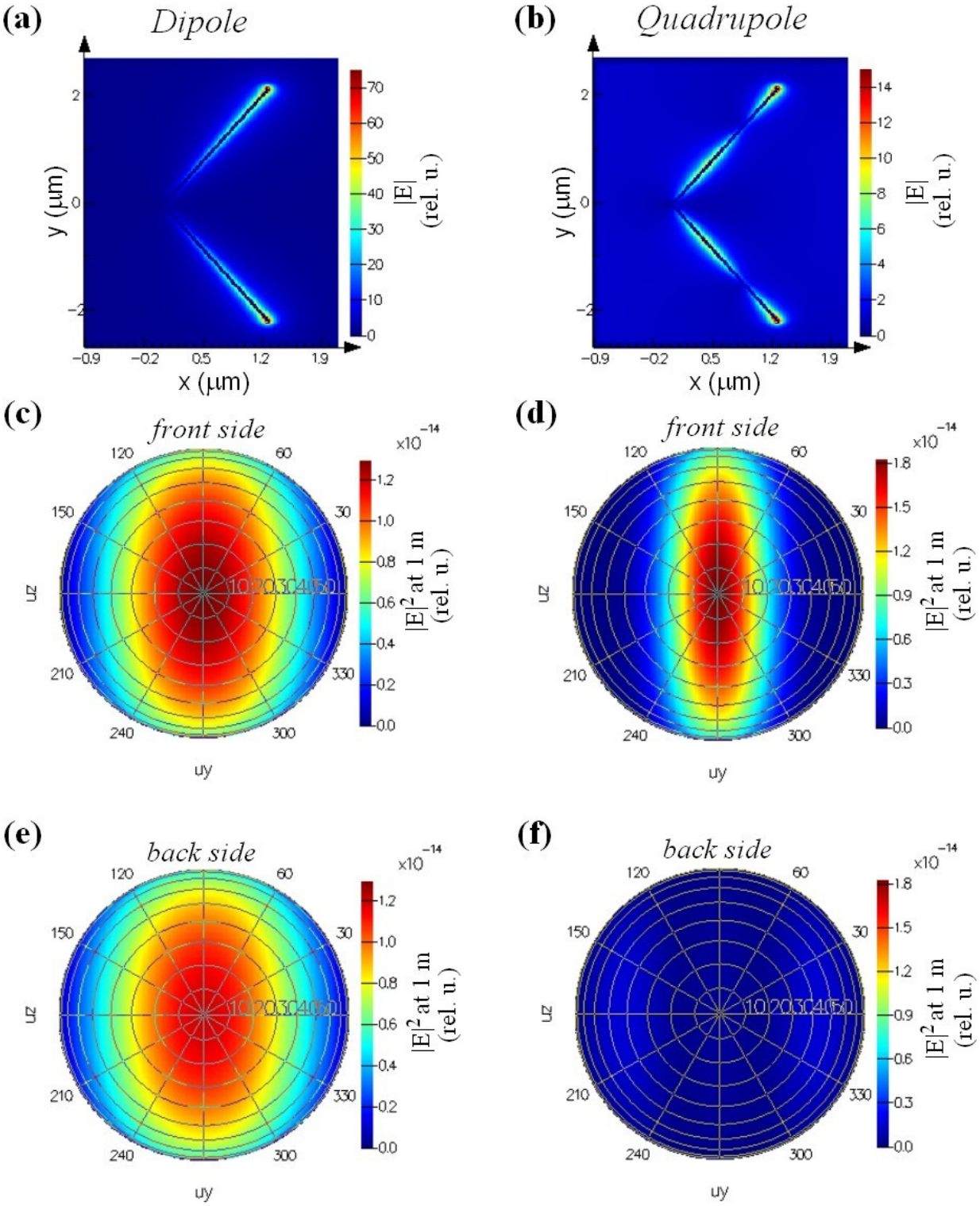

Figure 6.5: Visualization of electric field around the antenna when antenna dipole (a) or quadrupole (b) mode is excited. Angular dependence of light intensity scattered by the antenna into the front side half-space when dipole (c) or quadrupole (d) mode is excited. Angular dependence of light intensity scattered by the antenna into the back side half-space when dipole (e) or quadrupole (f) mode is excited.

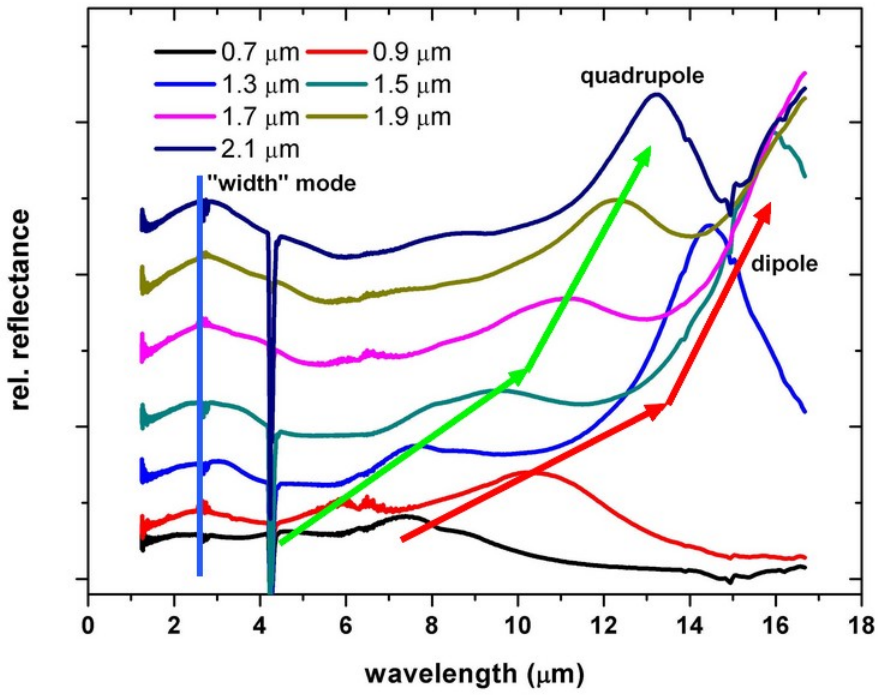

Figure 6.6: Experimental resonant spectra of gold V-antennas of various length (width 0.4 μm, height 0.06 μm) on silicon substrate. Green and red arrows indicate the shift of quadrupole and dipole antenna mode with antenna length, respectively. As the antennas are relatively wide and unpolarized source of light is used, the transversal resonant mode of the antenna is also visible at approximately 2.7 μm.

Calcium fluoride (CaF_2) represents an ideal substrate for the detection of antenna quadrupole modes. Its low refraction index (n varies from 1.33 to 1.42 in mid-IR) makes it a bad reflector. Due to the same reason, the antennas of the same resonant wavelength as their counterparts on silicon have to be longer. And longer antennas mean another increase of detected signal. A relative reflectance spectrum of gold antenna ($L = 3.52\,\mu$m) on CaF_2 substrate with clearly visible peak of quadrupole mode is shown in Figure 6.7b.

Consequently, we replaced the FTIR MCT detector with focal plane array (FPA) detector which is capable of sample mapping. After the measurements of antenna array response by FPA detector in both the reflection and transmission configuration we processed the recorded data and generate maps (Figure 6.7c,d) showing the area under the quadrupole peak corrected on baseline. The integration interval employed in the map generation process was from 8 to 10 μm (Figure 6.7b). High intensity of the quadrupole peak makes the antenna array clearly visible in both maps.

These maps has given us an idea on the experimental determination of the directivity of the fabricated antenna arrays. A substrate of calcium fluoride will be covered with a thin film of higher refraction index. This film will act as multimode planar waveguide (similarly to silicon nitride in Section 6.1). V-shaped antennas fabricated on top of the planar waveguide will couple the incoming light into the waveguide and grating outcouplers, tuned for the wavelength, where the directivity of the antenna is the biggest (will be numerically calculated), will be fabricated all around the antenna array. The gratings will

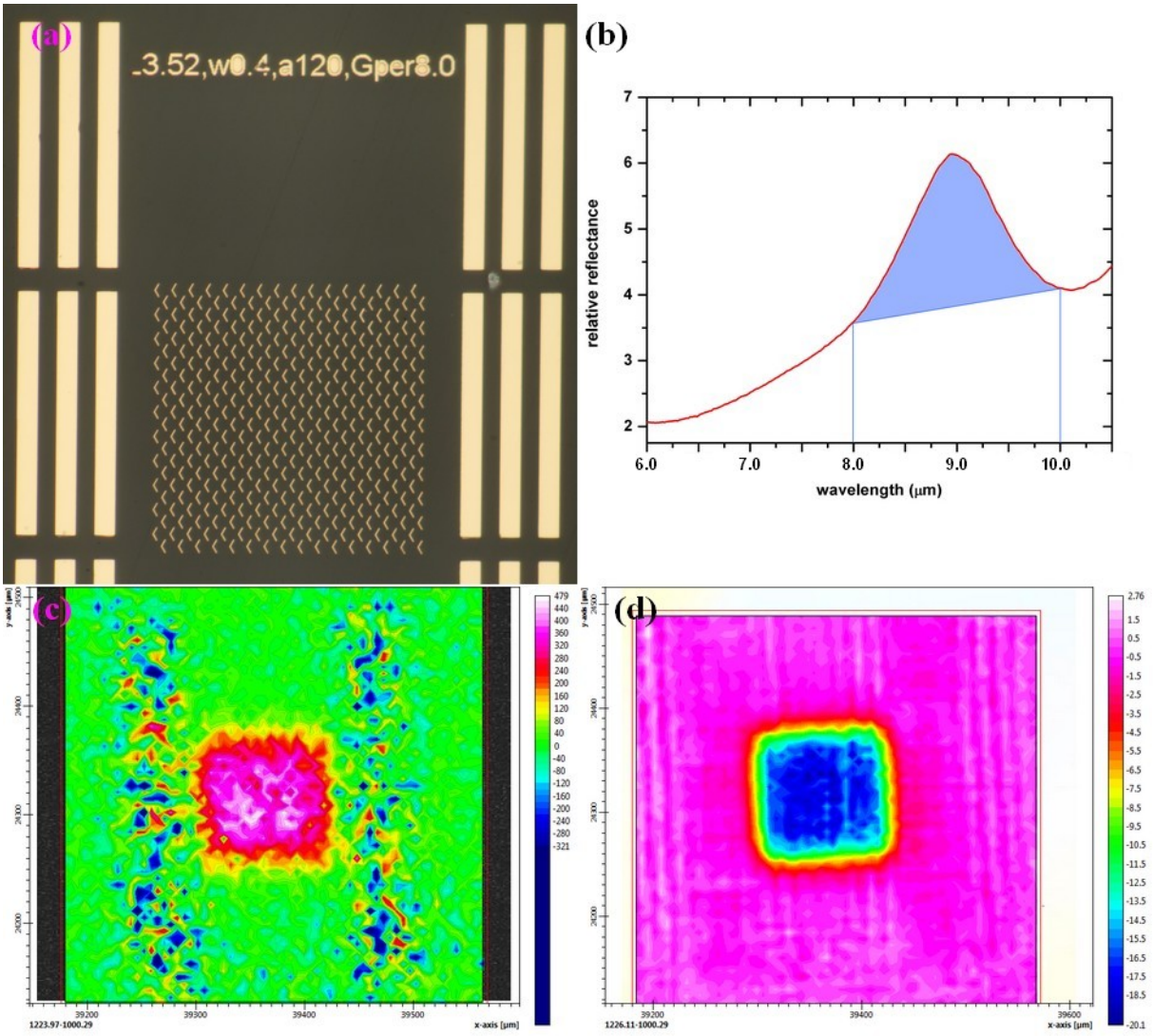

Figure 6.7: (a) Bright field microscope (Olympus MX51) image of a fabricated array of V-shaped antennas ($L = 3.52\,\mu$m) on CaF_2 substrate. (b) Part of the experimental reflectance spectra of the array showing the peak of antenna quadrupole mode, as recorded by integral MCT detector. The blue area from 8 to 10 μm marks the integration range in the map of signal intensity for quadrupole peak recorded by focal plane array (FPA) detector of micro-FTIR in reflection (c) and in transmission configuration (d).

outcouple the scattered light from the planar waveguide and direct it into the collection objective and FPA detector. This procedure should enable us do directly map the planar radiation pattern of antenna arrays.

7 Conclusion

In the presented thesis, the resonant properties of plasmonic antenna were studied both theoretically and experimentally. Theoretical calculations were performed in Lumerical FDTD Solutions software employing finite-difference time-domain numerical method. For the measurements, antennas were fabricated by electron beam lithography. The resonant properties of fabricated antennas were studied mainly by Fourier transform infrared spectroscopy. In this thesis, three topics were studied. The first study was devoted to the resonant properties of gold plasmonic antennas situated on nanocrystalline diamond film. The second one deals with the application of gold plasmonic antennas on silicon substrate as a plasmon based sensor of streptavidin. Finally, the emission directivity of V-shaped antenna quadrupole mode was investigated.

Resonant properties of gold plasmonic antennas situated on nanocrystalline diamond film were investigated in near-infrared region. The samples consisted of glass substrate, gold antennas, and several configurations of the nanocrystalline diamond layers or segments. The results can be summarized in following way. Due to higher refractive index of nanocrystalline diamond, the resonances of the antennas with diamond are red-shifted with respect to the case of bare glass substrate. The red-shift is accompanied by the lower values of antenna scattering cross section. The decrease in scattering cross section can be partly negated by appropriate tuning of the nanocrystalline diamond film thickness. The largest enhancement of the near field was obtained for a configuration with the antenna on a diamond film. The near-field is also more confined to the antenna-diamond interface and its decay from the boundary is faster than in the case of antenna-glass interface. Preliminary results on this topic were presented by the author in the form of poster at Diamond 2011, International Conference on Diamond and Carbon Materials in September 2011 and at NFO 12, Near Field Optics conference in September 2012. Soon, a paper on this topic will be submitted to a peer-reviewed journal.

In the second study we have demonstrated that the plasmonic antennas are sensitive to the optical properties of their surroundings. The resonant wavelength of fabricated antenna arrays shifted in the presence of a single layer of self-assembly molecules and even in the presence of a single atomic layer of graphene. However, measured shifts of resonant wavelength are very small and more sensitive techniques have been presented in literature. Therefore, our technique requires significant improvements to become more practical. Nevertheless, our results in the field of biosensing were presented by the author in the form of oral contribution at IVC 19, International Vacuum Congress in September 2013.

Our simulations of V-shaped antennas demonstrated highly directional scattering of light at the wavelengths close to the antenna quadrupole mode. In the experimental part of the study we showed that these V-antennas can be used as directional couplers for coupling the incoming light into waveguides. In such configuration, we achieved the antenna directivity up to 7 dB in near-infrared spectral region. Theoretical investigation of V-antenna directivity in mid-infrared region showed that for narrow V-antennas their directivity reaches approximately 10 dB and drops with increasing antenna width. We also showed that a careful selection of substrate can increase the signal detected from the antenna quadrupole mode and facilitate its experimental detection.

References

[1] NOVOTNY, L. The History of Near-field Optics. In *Progress in Optics*, vol. 50. Amsterdam: Elsevier, 2007. ISBN 978-0-444-53023-3. Chapter 5, p. 137–184.

[2] MIE, G. Beiträge zur Optik trüber Medien, speziell kolloidaler Metallösungen. *Ann. Phys. (Berlin)*, 1908, vol. 330, no. 3, 377–445.

[3] HORVATH, H. Gustav Mie and the scattering an absorption of light particles: Historic developments and basics. *J. Quant. Spectrosc. Radiat. Transf.*, 2009, vol. 110, 787–799.

[4] MÜHLSCHLEGEL, P. et al. Resonant optical Antennas. *Science*, 2005, vol. 308, 11607–11609.

[5] CROZIER, K. B. et al. Optical antennas: Resonators for local field enhancement, *J. Appl. Phys.*, 2003, vol. 94, p. 4632–4642.

[6] BOHREN, C. F., HUFFMAN, D. R. *Absorption and scattering of light by small particles*. New York: Wiley, 1983, 530 p., ISBN 04-710-5772-X.

[7] MAIER, S. A. *Plasmonics: Fundamentals and Applications*, 1st ed., New York: Springer, 2007. 224 p. ISBN 987-0-387-37825-1.

[8] NOVOTNY, L. Effective Wavelength Scaling for Optical Antennas. *Phys. Rev. Lett.*, 2007, vol. 98, 266802.

[9] KALOUSEK R. et al: Response of plasmonic resonant nanorods: an analytical approach to optical antennas. *Opt. Express*, 2012, vol. 20, no.16, 17916–17927.

[10] *FDTD - The Yee Cell* [online]. [cit. 2015-09-27]. <http://fdtd.wikispaces.com/The+Yee+Cell>.

[11] TAFLOVE, A. Application of the Finite-difference time-domain method to sinusoidal steady state electromagnetic penetration problems. *IEEE Trans. Electromagn. Compat.*, 1980, vol. 22, no. 3, 191–202.

[12] YEE, K. S. Numerical Solution of the initial boundary value Problems involving Maxwell's equation in isotropic Media. *IEEE Trans. Antennas. Propag.* 1966, AP-14, 302–307.

[13] *Lumerical Knowledge Base* [online]. Lumerical Solutions, Inc. ©2003-2015, [cit. 2015-09-13]. <http://docs.lumerical.com/en/index.html>.

[14] *FDTD Solutions* [online]. Lumerical Solutions, Inc. ©2003-2015, [cit. 2015-09-12]. <http://www.lumerical.com/tcad-products/fdtd>.

[15] YAGGI, N., VIJ, D.J. Fourier transform infrared spectroscopy. In *Handbook of Applied Solid State Spectroscopy*. New York: Springer, 2006, 741 p., ISBN 987-0-387-32497-5. Chapter 9, p. 410–450.

[16] MAIER, S. A., KIK, P. G., ATWATER, H. A. Obseravation of coupled plasmon-polariton modes in Au nanoparticle chain waveguides of different lengths: Estimation of waveguide loss. *Appl. Phys. Lett.*, 2002, vol. 81 , 1714–1716.

[17] MASS, T. W. W., TAUBNER, T. Incident Angle-Tuning of Infrared Antenna Array Resonances for Molecular Sensing. *ACS Photonics*, 2015, Article ASAP, DOI:10.1021/acsphotonics.5b00399.

[18] LUO, D. The road from biology to material. *Mater. Today*, 2003, vol. 6, no. 11., 38–43.

[19] KEDEM, O., TESLER, A. B., VASKEVICH A. et al: Sensitivity and Optimization of Localized Surface Plasmon Resonance Transducers. *ACS Nano* 2011, 5, 748–760.

[20] ARANGO, B. F., KWADRIN, A., KOENDERINK, A. F. Plasmonic Antennas Hybridized with Dielectric Waveguides. *ACS Nano*, 2012, vol. 6, no. 11, 10156–10167.

[21] FÉVRIER, M. et al. Giant Coupling Effect between Metal Nanoparticle Chain and Optical Waveguide. *Nano Lett.*, 2012, vol. 12, 1032–1037.

[22] VERCRUYSSE, D. et al. Unidirectional Side Scattering of Light by a Single-Element Nanoantenna. *Nano Lett.*, 2013, vol. 13, 3843–3849.

[23] BALANIS, C. A. *Antenna Theory: Analysis and Design.* Hoboken: John Wiley & Sons, 2005. 1050 p. ISBN 0-471-66782-X.

[24] VERCRUYSSE, D. et al. Directional Fluorescence Emission by Individual V-Antennas Explained by Mode Expansion. *ACS Nano*, 2014, vol. 8, 8232–8241.